Growth and Characterization of Cesium-Antimonide Photocathodes

by

Pallavi Saha

A Dissertation Presented in Partial Fulfillment
of the Requirement for the Degree
Doctor of Philosophy

Approved April 2023 by the
Graduate Supervisory Committee:

Siddharth Karkare, Chair
Peter Bennett
Robert Nemanich
Robert Kaindl

ARIZONA STATE UNIVERSITY

May 2023

ABSTRACT

The performance of kilometer-scale electron accelerators, which are used for high energy physics and next-generation light sources as well as meter-scale ultra-fast electron diffraction setups is limited by the brightness of electron sources. A potential emerging candidate for such applications is the family of alkali and bi-alkali antimonides. Much of the physics of photoemission from such semiconductor photocathodes is not fully understood even today, which poses a hindrance to the complete exploration and optimization of their photoemission properties. This thesis presents the theoretical and experimental measurements which lead to advances in the understanding of the photoemission process and properties of cesium-antimonide photocathodes.

First, the growth of high quantum efficiency (QE), atomically smooth and chemically homogeneous Cs_3Sb cathodes on lattice-matched strontium titanate substrates (STO) is demonstrated. The roughness-induced mean transverse energies (MTE) simulations indicate that the contribution to MTE from nanoscale surface roughness of Cs_3Sb cathodes grown on STO is inconsequential over typically used field gradients in photoinjectors.

Second, the formulation of a new approach to model photoemission from cathodes with disordered surfaces is demonstrated. The model is used to explain near-threshold photoemission from thin film Cs_3Sb cathodes. This model suggests that the MTE values may get limited to higher values due to the defect density of states near the valence band maximum.

Third, the detailed measurements of MTE and kinetic energy distribution spectra along with QE from Cs_3Sb cathodes using the photoemission electron microscope are presented. These measurements indicate that Cs_3Sb cathodes have a work function in the range of 1.5-1.6 eV. When photoemitting near this work function energy, the MTE nearly converges to the thermal limit of 26 meV. However, the QE is extremely low, of the order of 10^{-7}, which limits the operation of these photocathodes for high current applications.

i

Lastly, the growth of Cs_3Sb cathodes using the ion beam assisted molecular beam deposition (IBA-MBE) technique is demonstrated. This technique has the potential to grow epitaxial Cs_3Sb cathodes in a more reproducible, easier fashion. Structural characterization of such cathodes via tools such as reflection high energy electron diffraction (RHEED) and x-ray diffraction (XRD) will be necessary to investigate the role of the IBA-MBE technique in facilitating the epitaxial, ordered growth of alkali-antimonides.

To my family for their unconditional love and support...

ACKNOWLEDGEMENTS

TABLE OF CONTENTS

LIST OF TABLES

LIST OF FIGURES

Figure

Page

Chapter 1

INTRODUCTION

1.1   Photocathodes

Photocathodes are materials which emit electrons when illuminated with electromagnetic radiation such as light. Although the photoelectric effect was discovered as early as 1887 by Hertz [Hertz (1887)], it was not until 1905 that the concept of photoemission was explained by Einstein as a quantum effect, which won him the Nobel Prize. Since the discovery of photoemission, photocathodes have been extensively used in photon detection devices such as photomultiplier tubes and night vision goggles.

Over the last couple of decades, photocathodes have emerged as potential electron sources, which can drive various accelerator-based applications like X-Ray Free Electron Lasers (XFEL) [Emma *et al.* (2010)], Ultrafast Electron Diffraction/Microscopy (UED/UEM) [Lobastov *et al.* (2005); Sciaini and Miller (2011)], Electron-Ion Colliders (EIC) [Michizono (2019)] and Energy Recovery Linacs (ERL) [Gruner *et al.* (2002)]. Such accelerator applications have revolutionized the way dynamics of different ultrafast physical, chemical and biological processes, and structures of complex matter like viruses and proteins can be studied, at the atomic scale. A key figure of merit in the performance of such revolutionary instruments is the brightness of electron sources, which are used to drive such applications.

Typically for these applications a photoinjector is used, which consists of a photocathode placed in a DC or an RF electric field [Rao and Dowell (2013)]. A pulsed laser is used to extract electron bunches from the photocathodes, which are then accelerated by the electric field gradient to generate a beam of electrons. These electron beams are used to drive the aforementioned applications.

Such applications require the photocathodes to satisfy several requirements which are listed as follows:

1.1.1   High Quantum Efficiency

Quantum efficiency (QE) is defined as the ratio of the number of photoelectrons emitted (n_e) to the number of photons incident (n_p) on the photocathode. It can be calculated via the following equation:

$$\text{QE} = \frac{n_e}{n_p} = \frac{I/e}{P/h\nu},\tag{1.1}$$

which in more practical units reduces to:

$$\text{QE}[\%] = 1240\frac{I[A]}{P[W]\lambda[nm]},\tag{1.2}$$

where I is the measured photocurrent, e = $1.6\text{x}10^{-19}$ C is the electronic charge, P is the measured laser power, Planck's constant h = 6.626×10^{-34} Js, and ν and λ are the frequency and wavelength of incident light respectively.

For photon detection applications, QE is the single most important figure of merit. QE is often used as a metric to monitor the quality of photocathodes, for example alkali-antimonides during growth. High current applications like Energy Recovery Linacs and Electron Ion Colliders require photocathodes with QE greater than 1% in the visible light in order to use lasers with practically achievable power. Low current applications like Ultrafast Electron Diffraction and Free Electron Lasers, however, do not require high QE and can use photocathodes with QE lower by several orders of magnitude.

1.1.2   Low Mean Transverse Energy

Another important parameter which determines the performance of photocathodes for accelerator applications is the Mean Transverse Energy (MTE) or intrinsic emittance of

2

the cathode. MTE is the average kinetic energy of the photoemitted electrons in a direction perpendicular to their emission i.e. along the cathode's surface. It is related to the momenta and velocities in the transverse x and y directions in the following manner:

$$\text{MTE} = \frac{p_\perp^2}{2m_e} = \frac{1}{2}m_e[v_x^2 + v_y^2]. \tag{1.3}$$

MTE is related to the intrinsic emittance $\varepsilon_{n,x}$ via the following relation:

$$\varepsilon_{n,x} = \sigma_x\sqrt{\frac{\text{MTE}}{mc^2}}, \tag{1.4}$$

where σ_x is the rms size of the emission area on the cathode or the laser spot size, m is the rest mass of a free electron and c is the speed of light.

MTE is a function of the photocathode material and its surface geometry, unlike intrinsic emittance which depends on the laser spot size etc. The brightness of electron beams generated from photocathodes is inversely proportional to the MTE of photoemitted electrons [Musumeci *et al.* (2018)]. It is thus important to minimize the MTE of electrons emitted from photocathodes to improve the brightness of electron sources.

Higher brightness electron beams will increase both the X-ray pulse energy and the maximum lasing photon energy in XFELs. For example in the case of the high energy upgrade of LCLS-II i.e. LCLS-II-HE, the maximum lasing photon energy with the existing electron beam brightness will be 12 keV [DOE (2017)]. However, with an increase in beam brightness by a factor of 25 (or, a reduction in emittance by a factor of 5), the maximum lasing photon energy could be increased to 20 keV, thereby increasing the scientific reach of this instrument. An increase in beam brightness would also enable the development of a more accessible, table-top compact XFEL. From the perspective of UED applications, the brightness of the electron beam sets an upper limit to the unit cell size for which the diffraction pattern can be resolved. Given the existing beam brightness, only inorganic crystals with a relatively smaller lattice constant of ≈ 1 nm can be studied due to the low

transverse coherence length of the electrons. Electron beams brighter by a factor of 25 will enable the study of larger crystals, for example proteins and macromolecular assemblies with lattice constants of several nanometers, thus greatly extending the frontiers of this technique.

1.1.3   Long Lifetime

Lifetime is a fundamental important property for a photocathode which is often defined as the amount of time in which the QE drops to 1/e of its initial value. Photocathode materials can be sensitive to residual gases in the vacuum chamber, e.g. any oxygen containing species like O_2, H_2O, CO_2 etc, due to which their lifetimes get significantly shortened [Rao and Dowell (2013)].

During operation, different factors like back streaming of ions due to the electron beam ionizing residual gases (known as ion back bombardment), rise in cathode temperature due to laser illumination, and back streaming of chemically contaminating species towards the cathode may adversely impact the lifetime of the photocathodes [Dowell *et al.* (2010)].

1.1.4   Short Response Time

Response time is defined as the amount of time it takes for the electrons excited by incident photons to get emitted from the cathode surface. Response time is a critical parameter for photoinjector applications as it determines the achievable bunch charge for a given laser intensity as well as the temporal shape of emitted electron bunches. It is desirable to have a prompt response time less than 1 ps for most photoinjector applications so that the electron beam's temporal profile reflects the laser temporal profile [Rao and Dowell (2013)].

1.2   Types of Photocathodes

Photocathodes can be broadly classified into two categories: metallic and semiconductor cathodes.

1.2.1   Metallic Photocathodes

Metal photocathodes are characterized by low quantum efficiency, small intrinsic emittance, fast response time (< 1 ps), long operational lifetime and robustness to vacuum conditions [Rao and Dowell (2013)]. Metals have a high work function and require a powerful ultraviolet (UV) laser for photoemission, which poses a practical operational challenge for various applications. Moreover, the low QE of metals limits their applicability to high average current applications like Energy Recovery Linacs. Nonetheless, the use of metallic photocathodes is widespread in applications where high average current is not a foremost design goal. They are the most robust amongst all photoemitters with a significantly less complex preparation process, and they are commonly used in most DC guns and different high gradient RF guns to generate high brightness beams. Metal photocathodes such as copper are the backbone of the BNL/SLAC/UCLA and LCLS s-band guns .

Some other examples of metallic photocathodes are pure metallic lead (Pb), niobium (Nb), magnesium (Mg), and silver (Ag).

1.2.2   Semiconductor Photocathodes

The next type of cathodes are semiconductor cathodes, which are broadly classified into the following two categories based on the location of the vacuum energy level:

(a) Positive Electron Affinity PEA cathodes: Examples include cesium-telluride Cs_2Te and the family of alkali- and bialkali- antimonides that includes Cs_3Sb, Na_2KSb, K_2CsSb etc. These cathodes are typically grown on substrates which have undergone treatment

prior to the growth process.

(b) Negative Electron Affinity NEA cathodes: Commercially available semiconductor cathodes like GaAs, GaN can be activated to a negative electron affinity (NEA) condition by coating them with a monolayer of Cs and an electronegative element such as O_2 [Bell (1973)]. Due to the deposition of a monolayer of volatile Cs at the surface, such cesiated cathodes are extremely sensitive to any oxygen containing species and can only be operated in extreme ultra high vacuum conditions (pressure $< 10^{-11}$ torr).

Semiconductor cathodes have higher QE than metallic cathodes in the UV-to-visible wavelength range, which has facilitated their successful use in high current applications. K_2CsSb cathode has demonstrated the highest achievable average current of 65 mA in a photoinjector intended for use in ERL [Dunham *et al.* (2013)]. However, these cathodes are not as robust to vacuum conditions as metals and have longer response time and reduced operational lifetimes.

An ideal photocathode must have high QE, preferably greater than 1% in the visible wavelengths, low MTE and exhibit long lifetime along with short response time (<1 ps). Unfortunately, no photocathode in existence today fulfills all the requirements simultaneously. Tradeoffs often have to be made between different operating conditions, e.g. for example laser wavelengths, in order to use a particular photoemissive material for a given application [Dowell *et al.* (2010)]. For example, GaAs surfaces activated using Cs and NF_3 exhibit an MTE as low as 25 meV in the infrared wavelengths, however with large response time (> 10 ps) which makes them inefficient for ultrafast accelerator applications. By operating the same cathode with green-wavelength excitation, electron bunches with low response time (< 2 ps) can be obtained, which is however at the cost of undersirable MTE (> 120 meV) [Bazarov *et al.* (2008)]. In the next section, we discuss how the family of alkali-antimonides fulfills the various conflicting requirements of a photocathode to a reasonably good extent.

1.3 Alkali-antimonide Photocathodes

Alkali-antimonides have emerged as popular candidates for the electron sources to drive the next generation light sources, electron cooling of hadron beams and electron-ion collider experiments. This is due to a multitude of reasons. Alkali-antimonides yield a QE greater than 1% and reasonably low MTE in the visible wavelengths, demonstrate long operational lifetimes and quite low response time [Rao and Dowell (2013); Musumeci *et al.* (2018); Dowell *et al.* (2010)]. In the dissertation, I will concentrate on the study of cesium-antimonide (Cs_3Sb) photocathodes. Characterized by three Cs atoms and one Sb atom per unit cell, these cathodes have a low band gap energy E_g and electron affinity E_a.

Alkali-antimonides like Cs_3Sb, Na_2KSb and K_2CsSb have been successfully used in photoinjectors to achieve very high average beam currents approaching 100 mA, due to their very high quantum efficiency ($>1\%$) in visible (green) light for energy recovery linac applications [Dunham *et al.* (2013); Schmeißer *et al.* (2018); Vecchione *et al.* (2011)]. These materials have higher QE than metals and photoemit electrons via visible light excitation which makes the spatio-temporal manipulation of photoemission laser pulses easier. Such traits make alkali-antimonides very attractive candidates for FELs and UED applications, whose performance is largely limited by the mean transverse energies (MTE) of emitted electrons.

With the goal of minimizing the MTE [Cultrera *et al.* (2015)] and achieving the highest possible brightness in the photoinjector, the MTE and QE performance of Cs_3Sb close to the photoemission threshold (wavelength range of 600 nm-700 nm) has been investigated at both room and cryogenic temperatures. The smallest MTE measured from Cs_3Sb films was 40 meV at room temperature and 22 meV at 90 K - significantly larger than the thermal limit of 25 meV at room temperature and 8 meV at 90 K [Cultrera *et al.* (2015)]. This discrepancy/difference between the theoretical and experimentally measured values of

MTE baffled the photocathode community, which led to considerable efforts to mitigate the larger than thermal limit MTE values. The primary reasons, which could potentially result in larger MTE, were identified to be the surface roughness and work function variations of the alkali-antimonide photocathodes and bulk defect density of states. While effects of surface roughness on the MTE have been investigated theoretically in great detail [Feng *et al.* (2017); Smedley *et al.* (2015); Karkare and Bazarov (2015); Gevorkyan *et al.* (2018)], the impact of intra-band gap defect states on MTE has never been systematically investigated.

In Chapter 2, we first discuss how the surface roughness and work function variations at the surfaces of cathodes can cause the MTE of electrons emitted from them to increase. After briefly discussing the past attempts directed at reduction of surface roughness induced MTE, we demonstrate that high QE Cs_3Sb cathodes grown on lattice-matched strontium titanate (STO) substrates have a factor of 4 smoother and chemically uniform surfaces compared to those traditionally grown on Si substrates. We perform simulations to calculate roughness induced MTE based on the measured topographical and surface-potential variations on the Cs_3Sb films grown on STO, and we show that these variations are small enough to have no consequential impact on the MTE and thus, the brightness of electron beams.

Chapter 3 is dedicated to a new approach that we have developed to model photoemission from cathodes with disordered surfaces, within the framework of Spicer's three step model. This model can be used to explain photoemission from all real cathodes which are typically used in photoinjectors, be it metals or semiconductors. In our work, we have used the semiconductor model to explain near threshold photoemission from thin film Cs_3Sb photocathodes. Our model predicts values of QE and MTE, which are in excellent agreement with those measured experimentally at both room temperature and cryogenic temperature. Our model suggests that the MTE from such polycrystalline Cs_3Sb cathodes may not approach the thermal limit, when operated near the photoemission threshold.

We have thus far discussed the various factors that can influence the MTE from Cs_3Sb

8

cathodes, without presenting any MTE measurement. Due to the high susceptibility of Cs₃Sb cathodes to moisture and any oxygen-containing species, coupled with the complexities of the measurement processes, there is a lack of complete, detailed measurements of the photoemission properties (QE, MTE and kinetic energy distribution spectra) of alkali-antimonide cathodes.

Chapter 4 is dedicated to the investigation of the kinetic energy distribution data and MTE from the Cs_3Sb cathodes using the photoemission electron microscope (PEEM). The kinetic energy distribution spectra indicate a work function of the Cs_3Sb cathodes ~ 1.5 eV, which is significantly lower than previously perceived values of 1.8-2.0 eV based on the knee-like feature observed in QE spectral response plots. Further, our measurements show that the MTE converges nearly to the thermal limit of k_BT of 25 meV at room temperature when operated at the actual threshold. Moreover, at 1.8 eV, the MTE was measured to be 40 meV which is comparable to the previously reported value. This higher-than-k_BT value of MTE is not due to surface roughness effects as was previously thought, but it is simply a consequence of excess energy at 1.8 eV. However, the QE of the Cs_3Sb cathodes is very low, of the order of 10^{-7} at the threshold. As a result, the cathodes may need to be operated at photon energies away from the threshold, which would lead to higher MTE as a consequence of higher excess energy. Epitaxial, single-crystalline Cs_3Sb cathodes and other alkali-antimonides may, however, exhibit different photoemission features when operated at the threshold.

Although single-crystalline epitaxial Cs_3Sb cathodes have been demonstrated by [Parzyck *et al.* (2022)], the growth process is fairly complex and involves a two-step process of low temperature deposition and high temperature annealing. Moreover, it is non-trivial to achieve reproducibility of growth via this technique. Furthermore, the defect density in the bulk and the surface roughness achieved from this growth process are also not well understood. This emphasizes the need for a more reproducible and simpler technique for

the growth of single-crystalline, epitaxial alkali-antimonide photocathodes.

One significant factor which could potentially hinder an epitaxial growth of alkali-antimonides (for example, Cs_3Sb) performed via thermal evaporation of sources, is a surface mobility mismatch between the constituent atomic species. For many epitaxial films, high surface mobility is often achieved by using a high substrate temperature in the several 100°C range. However, the dissociation temperature of Cs_3Sb films is well below 250°C [Ding *et al.* (2017)] and hence, the growth has to be performed at significantly lower substrate temperatures in the several 10°C range. These lower temperatures put a severe constraint on the mobility of antimony atoms.

An alternate method to improve surface mobility and reconstruction without raising the substrate temperature is the ion-beam-assisted molecular-beam-epitaxy (IBA-MBE) technique. In this technique, the growing film is irradiated with hyperthermal ions (E > 1 eV) along with low thermal energy atoms (E < 1 eV). This stimulates the growth via ballistic enhancement of mobility [Trushin *et al.* (2008)]. The underlying idea behind this technique is that the hyperthermal ion bombardment imparts enough energy to overcome the surface displacement energy but not the bulk displacement energy.

Chapter 5 is devoted to the demonstration of growth of Cs_3Sb cathodes with a reasonably high QE via IBA-MBE technique. Instead of routinely used thermal Cs sources in the form of SAES strips [SAE (2023)], alkali-azides [Cultrera *et al.* (2014)], pure metallic Cs [Cultrera *et al.* (2016)], SAES alkali metal dispenser [Feng *et al.* (2017)] and SAES cesium molybdate pellets [Saha *et al.* (2022)], we have used a hyperthermal Cs^+ ion gun designed and manufactured by Kimball Physics. Bombardment of the growing film with energetic Cs^+ ions provides hyperthermal kinetic energies, which can improve the antimony mobility without the need to raise the substrate temperature.

Chapter 2

PHYSICALLY AND CHEMICALLY SMOOTH CESIUM-ANTIMONIDE PHOTOCATHODES ON SINGLE CRYSTAL STRONTIUM TITANATE SUBSTRATES

This chapter was originally published as Ref. Saha *et al.* (2022).

2.1 Abstract

The performance of X-ray Free Electron Lasers and Ultrafast Electron Diffraction experiments is largely dependent on the brightness of the electron sources from photoinjectors. The maximum brightness from photoinjectors at a particular accelerating gradient is limited by the Mean Transverse Energy (MTE) of the electrons emitted from the photocathodes. For high Quantum Efficiency (QE) cathodes like alkali-antimonide thin films, which are essential to mitigate the effects of non-linear photoemission on MTE, the smallest possible MTE and hence the highest possible brightness is limited by the nanoscale surface roughness and chemical inhomogeneity. In this work, we show that high QE Cs_3Sb films grown on lattice-matched strontium titanate (STO) substrates have a factor of 4 smoother, chemically uniform surfaces compared to those traditionally grown on disordered Si surfaces. We perform simulations to calculate roughness-induced MTE based on the measured topographical and surface-potential variations on the Cs_3Sb films grown on STO and show that these variations are small enough to have no consequential impact on the MTE and hence the brightness.

2.2 Introduction

The brightness of electron beams is a key figure of merit for state-of-the-art ultrafast science tools such as X-ray Free Electron Lasers (XFELs) and Ultrafast Electron Diffrac-

11

tion/ Microscopy (UED/UEM) experiments. An increase in the electron beam brightness can lead to the generation of higher power and shorter wavelength x-ray pulses in existing XFELs [Ferrario (2015)] as well as enable the development of compact XFELs [Rosenzweig *et al.* (2020)]. From the perspective of UED applications, higher beam brightness will cause an increase in the spatiotemporal resolution and allow the study of crystals with larger lattice sizes, enabling groundbreaking research in the ultrafast study of quantum materials and critical chemical and biological processes [Oudheusden *et al.* (2007)].

High density bunched electron beams for the above applications are typically produced using photoinjectors which consist of a photoemissive surface (photocathode) placed in an accelerating electric field (E) along with electron optics to mitigate the brightness-degrading effects of space charge. The accelerating electric field is typically in the range of a few to 100 MV/m depending on the design of the photoinjector and the required application [Musumeci *et al.* (2018)].

For most photoinjectors the maximum achievable brightness scales according to the following relation:

$$B \propto \frac{E^n}{\text{MTE}}, \tag{2.1}$$

where n is a real number between 1 and 2 depending on the design of the photoinjector and MTE is the mean transverse energy of the electrons emitted from the photocathode.

The Mean Transverse Energy (MTE) can be related to the normalized transverse emittance $\varepsilon_{n,x}$ from the photocathode via the relation:

$$\varepsilon_{n,x} = \sigma_x \sqrt{\frac{\text{MTE}}{mc^2}}, \tag{2.2}$$

where σ_x is the rms size of the emisison area on the cathode, m is the rest mass of a free electron and c is the speed of light.

Typically, the maximum possible accelerating electric field is set by the design of the photoinjector, however, the MTE is a function of the photocathode material, its surface and

the photon energy used for emission. Hence minimizing the MTE from photocathodes is critical for maximizing the electron beam brightness from photoinjectors. For a typical bunch charge, the smallest possible MTE (and hence highest brightness) is limited to a few meV due to point-to-point electron interactions [Gordon *et al.* (2021)] and disorder induced heating of the electron bunch [Maxson *et al.* (2013)].

The MTE from the cathode is typically proportional to one third of the excess energy (energy difference between the incident photon energy and the work function of the cathode surface) [Dowell and Schmerge (2009)]. However, for low or negative excess energy the MTE becomes limited by the Fermi tail of the electron distribution to k_BT, where k_B is the Boltzmann constant and T is the lattice temperature of the cathode [Vecchione *et al.* (2013)]. This thermal limit has been experimentally demonstrated for thin polycrystalline Sb films at room temperatures resulting in an MTE of 25 meV [Feng *et al.* (2015)]. Reduction in MTE down to 5 meV from the Cu(100) surface cooled to cryogenic temperatures has also been demonstrated [Karkare *et al.* (2020)]. However, such metal cathodes have an extremely low Quantum Efficiency (QE), typically less than 10^{-6}-10^{-8} at threshold photon energies. Hence, a large laser fluence is required to extract the charge densities required for the various XFEL and UED photoinjector applications. The large laser fluence conditions result in MTE of few 100 meV due to non-linear photoemission effects of laser heating [Maxson *et al.* (2017)] and multiphoton emission [Bae *et al.* (2018); Knill *et al.* (2021)].

One way to mitigate the MTE-degrading effects of non-linear photoemission is to use high-QE, low-electron-affinity semiconductor cathodes like alkali-antimonides. Such cathodes don't require very large laser fluence to attain the required charge densities. Alkali-antimonides like Na_2KSb, K_2CsSb and Cs_3Sb have already been successfully used in photoinjectors to achieve very high average beam currents approaching 100 mA due to their very high quantum efficiency (>1%) in visible (green) light for energy recovery linac applications [Dunham *et al.* (2013); Schmeißer *et al.* (2018); Vecchione *et al.* (2011)]. The MTE

13

and QE performance of Cs_3Sb close to the photoemission threshold (wavelength range of 600 nm -700 nm) has also been investigated at both room and cryogenic temperatures, with the goal of minimizing the MTE [Cultrera *et al.* (2015)] and achieving the highest possible brightness in photoinjectors. The smallest MTE measured from Cs_3Sb films was 40 meV at room temperatures and 22 meV at 90 K - significantly larger than the thermal limit of 25 meV at room temperature and 8 meV at 90 K [Cultrera *et al.* (2015)]. This MTE above the thermal limit was attributed to the non-uniform nature of the Cs_3Sb surface. These measurements were performed at low electric fields well below 1 MV/m. Hence it is critical to produce alkali-antimonide films with minimal surface non-uniformities to maximize the brightness of electron beams.

Surface non-uniformities such as physical roughness and work function variations (often termed chemical roughness) can result in transverse accelerating fields close to the cathode surface increasing the MTE in photoinjectors. Nano-scale physical roughness on the cathode surface bends the accelerating electric field lines close to the surface resulting in transverse acceleration of the emitted electrons increasing the MTE. The resulting MTE increase is proportional to the accelerating electric field, the square of the amplitude of the roughness and inversely to the periodicity [Feng *et al.* (2017)]. Chemical roughness on the other hand produces transverse electric fields between regions with varying work functions. These electric fields also result in increased MTE, however, their effect on MTE reduces with increasing accelerating electric field [Karkare and Bazarov (2015)]. The combined effects of physical and chemical roughness from realistic cathode surfaces on MTE can result in a non-trivial, non-monotonic dependence of MTE on the accelerating electric field. This dependence can be obtained computationally by using a Fourier-like decomposition of the resultant electric field close to the surface and numerically tracking the trajectories of electrons in this field [Gevorkyan *et al.* (2018)].

In order to minimize the effects of physical and chemical roughness on MTE, there

has been a considerable effort undertaken to develop alkali-antimonide thin film growth techniques that result in minimal surface non-uniformities. The films that are grown using the traditional sequential process of first depositing several nm thick Sb film followed by the deposition of alkali metals at elevated temperatures results in a large roughness exceeding several nm rms with a spatial period of 100 nm [Schubert *et al.* (2013)]. Such films often result in unacceptably large roughness induced MTEs. A significantly smoother surface of alkali-antimonide films (with 0.6 nm rms roughness) was achieved by co-depositing the Sb and alkali-metals onto a Si substrate at elevated temperatures [Feng *et al.* (2017)]. The MTE increase per unit accelerating electric field $\Delta \text{MTE}/E = 0.5$ meV/(MV/m) due to the physical roughness was computed from the atomic force microscopy (AFM) measurements on such surfaces. Co-deposition of Cs and Sb on single crystal substrates like 3C-SiC (100), $Al_2O_3(10\bar{1}0)$, TiO_2 (001) that are lattice matched to Cs_3Sb , was investigated as a route toward achieving smoother, ordered surfaces of Cs_3Sb with reduced MTE [Parzyck *et al.* (2022)]. Among these lattice-matched substrates, 3C-SiC(100) resulted in the smallest physical roughness with $\Delta \text{MTE}/E$ ranging between 0.24-0.79 meV per MV/m. Even in the best case scenario of 0.24 meV/(MV/m) the MTE increase due to physical roughness at large accelerating gradients of 100 MV/m is comparable to that of the thermal MTE ($k_B T$) at room temperature and significantly exceeds it at cryogenic temperatures.

Despite the significant reduction in surface roughness of alkali-antimonide films, as stated above, the smoothest surfaces achieved will still result in non-negligible contribution to MTE at very large accelerating gradients when trying to achieve the smallest possible MTE. Moreover, the chemical roughness or work function variations on such alkali-antimonide films have not been measured in a reliable fashion. Such variations could dominate the roughness effect on MTE at smaller accelerating fields of < 20 MV/m and could explain the higher-than-thermal MTE measurements from Cs_3Sb at low electric fields [Cultrera *et al.* (2015)].

15

2.3 Experiment

STO(100) was chosen from an open-source list of 150 commercially available candidate substrates Paul *et al.* (2021), which are lattice-matched to Cs_3Sb using the MPInterfaces software package [Mathew *et al.* (2016)]. The (100) face of STO (lattice constant 3.93 Å) was found to have a 0.7 % lattice mis-match with Cs_3Sb (lattice constant 9.334 Å), with 3 unit cells of STO corresponding to 1 cubic unit cell of Cs_3Sb. Growth performed on a lattice matched surface could result in epitaxy with higher degree of crystallinity and thus may result in smoother films compared to those grown on disordered/non-lattice-matched substrates like Si or polished metals as demonstrated in this paper.

Cs_3Sb films were grown on both STO and Si substrates. Both STO and Si substrates were purchased from MTI Corp [MTI (2023)] and were atomically-flat, single-crystal, epi-ready substrates with a disordered native oxide formed on the surface. The STO substrate was p-doped with Nb dopants to a value of 0.05% by atomic weight, while the Si substrate was p-doped with boron atoms. Both STO and Si substrates were rinsed with isopropanol and annealed at 600 °C for two hours in an ultra-high-vacuum (UHV) growth chamber [Feng *et al.* (2017)] with a base pressure in the low 10^{-10} Torr range as is typically done prior to alkali-antimonide growth. For STO, this resulted in a well ordered, atomically smooth, pristine surface, that was confirmed by observing atomic steps/terraces with rms roughness of < 0.1 nm using the AFM. For Si, annealing at this temperature gives rise to an atomically smooth, but disordered surface with the native oxide layers and a AFM measured rms roughness of < 0.3 nm.

Cs_3Sb thin films were grown via co-deposition of Cs and Sb onto the substrates. During growth, the substrates were heated radiatively and held at a constant temperature of 75 °C. Sb was evaporated by heating 99.9999% pure Sb pellets (Alfa Aesar) [Sb- (2023)] and Cs was evaporated by heating cesium molybdate pellets (SAES Getters) [Cs- (2023)], placed

in their respective effusion cells [eff (2023)]. The Sb source is heated to 400 °C, which corresponds to a flux rate of 0.001 nm/s at the location of the substrate. This flux rate was pre-calibrated using a quartz crystal balance. Cs source temperature was set in the range of 350-450 °C, and was adjusted by a few degrees during the growth to maintain a constant Cs partial pressure of $(1.2 \pm 0.1) \times 10^{-10}$ torr, on a residual gas analyzer (RGA). The Cs source is located ~4 inches away from the substrate while the RGA was located in the growth chamber, but out of the direct line of sight of the Cs source.

During deposition the growth was monitored by measuring the QE of the film under illumination with a 532 nm CW laser. The substrates were held at a -30 V bias w.r.t the chamber walls and the current emitted from the substrate was measured using a picoammeter. Growth on both substrates was performed until the QE plateaued. At this point the samples were allowed to cool to room temperature. All the films yielded a high final QE between 2-5 % in the green, as typically expected from Cs_3Sb cathodes.

The QE plateau on the STO substrate was attained within a very short time period of ~15 min from the start of the deposition, while the films on Si typically took ~1.5 hours to plateau. Given the Sb deposition rate of 0.001 nm/s and a factor of 7 higher thickness of the Cs_3Sb film compared to the Sb film thickness [Hagino and Takahashi (1966)], the 15 min growth on STO corresponds to a very thin film of 6.3 nm and the film on the Si substrate was estimated to be ~40 nm thick. In order to compare the properties of films of equal thickness on the two substrates, a thick film was intentionally grown on the STO substrate as well. Although the QE plateaued on the STO substrate in ~15 min, growth was continued for ~1.5 hours to reach a thickness of ~ 40 nm, comparable to that of Si. During this period, the QE was largely constant and increased very slowly to a value of ~5 %.

Such thin (6.3 nm) films of Cs_3Sb with a QE >2 % in the green are atypical. However, recent results of epitaxially grown single crystalline Cs_3Sb films on 3C-SiC (100) have

demonstrated such low-thickness-high-QE behavior [Parzyck *et al.* (2022)]. The QE spectral response and surface non-uniformities (physical and chemical roughness) of the films were investigated. The QE spectral response was measured by monitoring the photocurrent emitted by the sample using a lock-in amplifier, while light from a pulsed Optical Parametric Amplifier (Light Conversion Orpheus pumped by Light Conversion Pharos) was incident on the sample surface. The fluence of the laser pulses incident on the sample was kept small enough to ensure linear photocurrent to avoid effects of space charge and non-linear photoemission. The physical and chemical roughness was measured using a UHV RHK-AFM instrument connected in UHV to the growth chamber. AFM-KPFM measurements are performed on the samples grown, in the frequency modulation mode by using Si tips coated with Cr/Pt suited for electrical measurements like KPFM . For the AFM measurements, the tip images the sample line by line via raster scanning the sample surface (x,y), while the frequency regulation feedback system maintains a constant frequency shift from the resonance by adjusting the tip-sample distance. The z-motion of the tip to maintain constant frequency shift is the measure of the physical roughness of the sample [Melitz *et al.* (2011)]. The force between the tip and the sample goes to a minimum when the electrical potential difference applied between them is equal to the contact potential difference. The contact potential difference (relative work function) between the sample and the conducting tip is measured by adding a small voltage oscillation to the sample bias and running a separate feedback loop to keep the force to a minimum during the AFM scan [Melitz *et al.* (2011)]. The electrical potential difference applied at each point during the raster then gives the KPFM image of the surface contact potential variation or the work function variation. Due to the larger height variations on the film on the Si substrate and the volatile nature of Cs_3Sb, it was not possible to obtain a reliable KPFM image. However, a very clear KPFM image of the films on STO substrate was obtained.

18
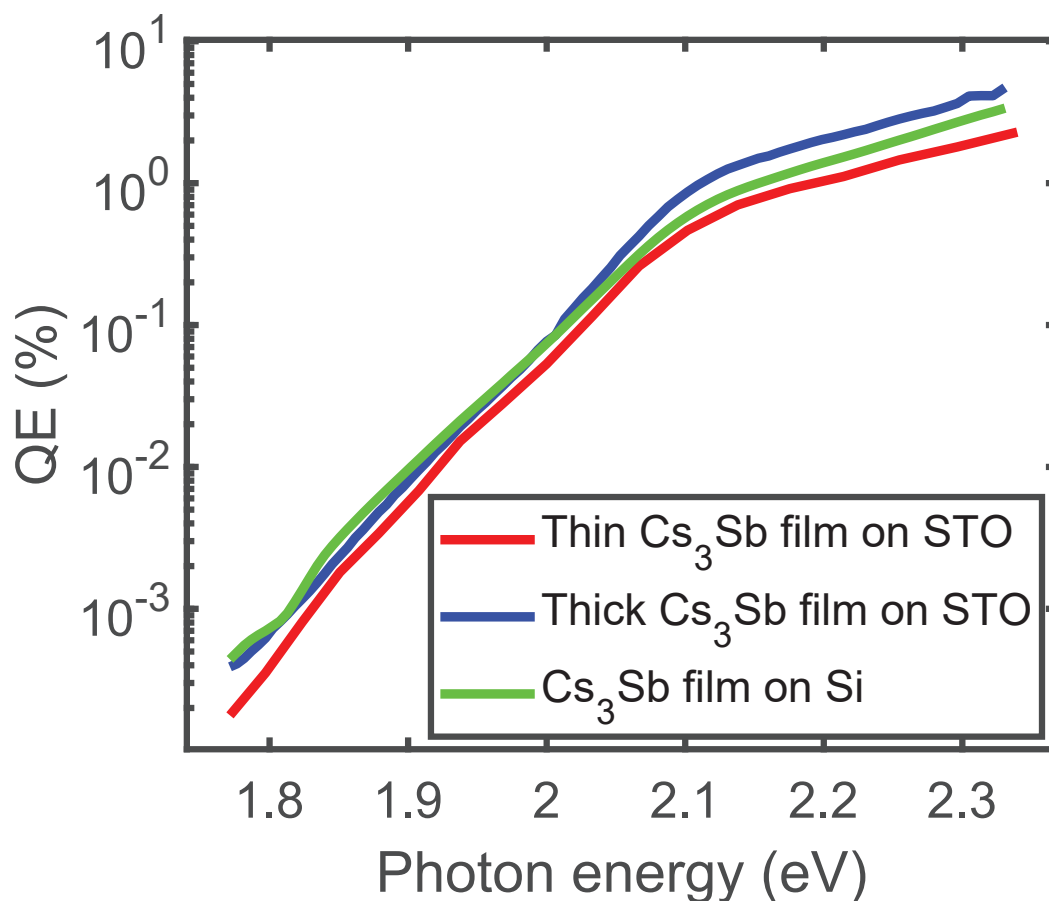
Figure 2.1: QE Spectral Response Measured from Cs_3Sb Photocathodes Grown on STO and Si Substrates.

The QE spectral response of the films is shown in Figure 2.1. The cathodes grown on different substrates exhibit similar profiles, QE ranging between 2-5 % in green light and a photoemission threshold near ~2.1 eV as indicated by the knee in the spectral response curve.

Fig. 2.2 shows the AFM images of the thin film (Fig. 2.2(a)), thick film (Fig. 2.2(b)) grown on STO and the film (Fig. 2.2(c)) grown on Si. Fig. 2.3 shows the KPFM images obtained on the thin film (Fig. 2.3(a)) and the thick film (Fig. 2.3(b)) on the STO substrate.
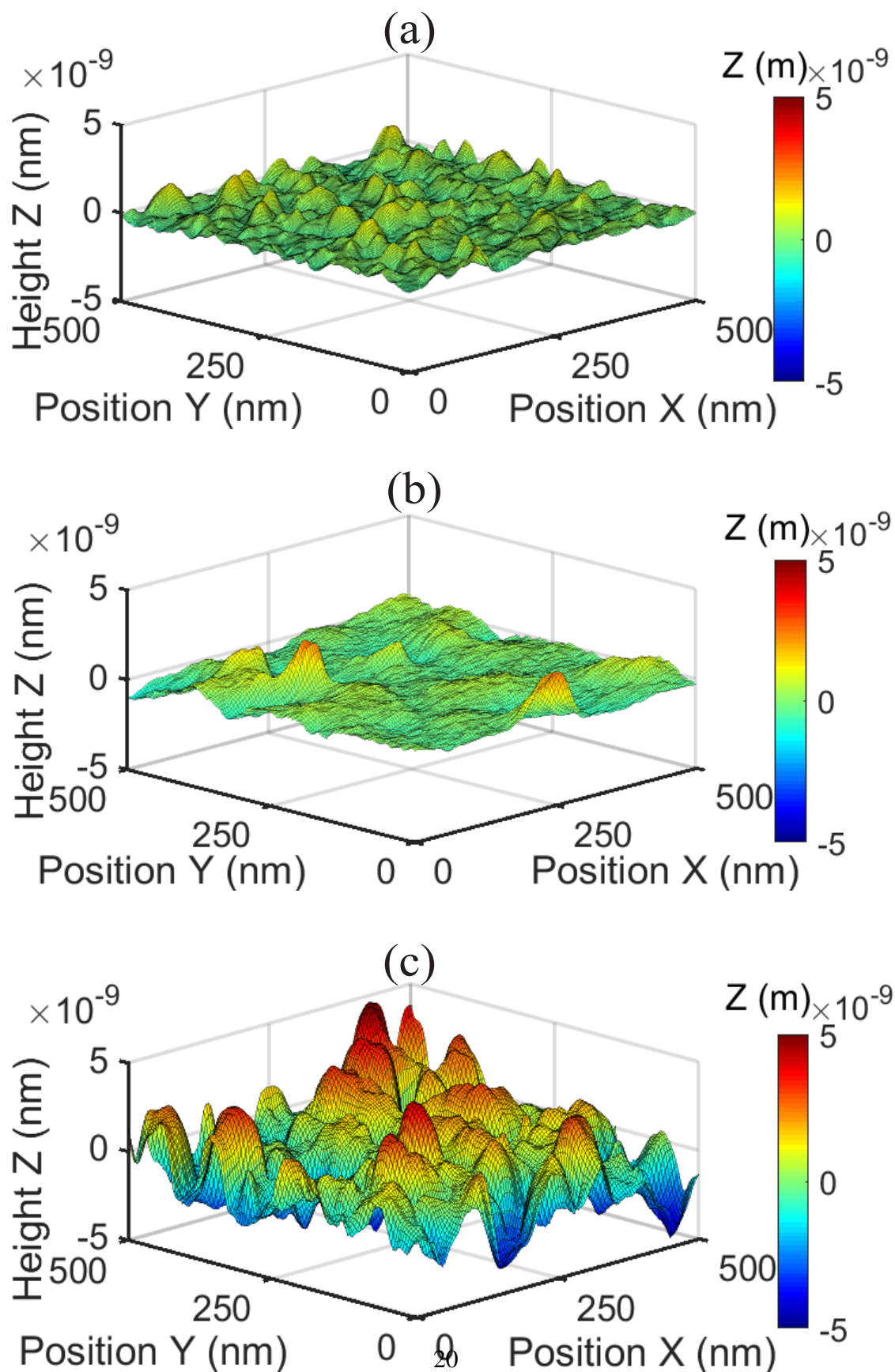
Figure 2.2: 3D Topography Images of (a) Thin Cs$_3$Sb Film on STO, (b) Thick Cs$_3$Sb Film on STO and, (c) Cs$_3$Sb Film on Si.
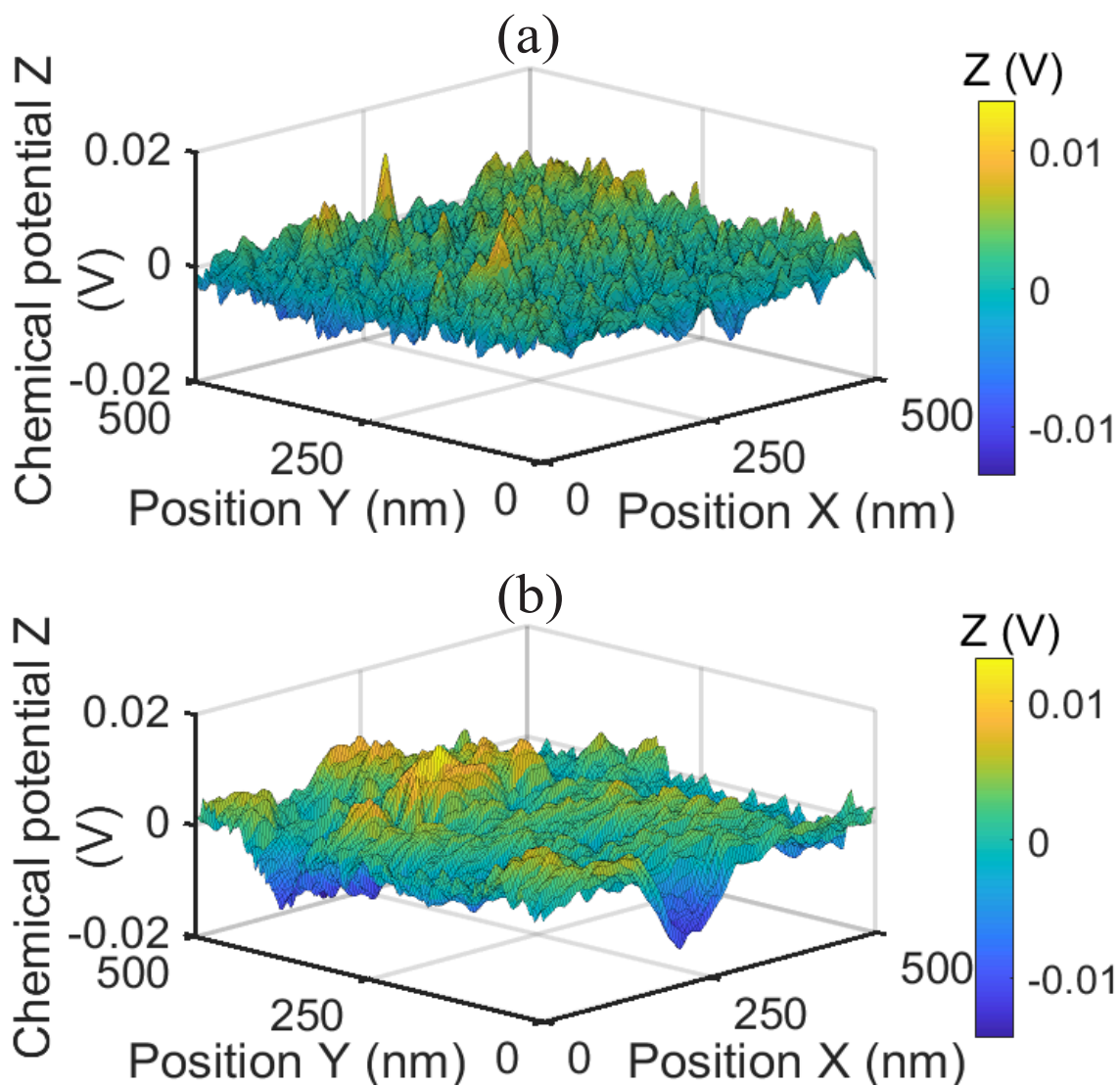
Figure 2.3: 3D Chemical Potential Maps of (a) Thin Cs_3Sb Film on STO and, (b) Thick Cs_3Sb Film on STO.

The KPFM images are taken during the AFM scan and hence represent the exact same area of the film surface.

The thin film on STO has the smallest out-of-plane rms surface roughness of 0.3 nm with an in-plane periodicity ~ 60 nm and a rms surface potential variation (chemical roughness) of 2.65 mV. The thick film on STO has a larger out-of-plane rms surface roughness of 0.6 nm with a larger in-plane periodicity ~ 100 nm and a rms surface potential variation of 4.32 mV. The film on Si has a significantly larger out-of-plane rms surface roughness of 1.4 nm (4 times larger than that of the thin film on STO) with a periodicity ~ 100 nm. The error associated with physical and chemical roughness measurements due to instrumental uncertainty has been estimated to be ~ 10 %.

In order to estimate the effects of these measured physical and chemical roughness on the MTE, the electric field close to the surface was calculated using a Fourier-like decomposition for various accelerating gradients. For the Si surface the surface potential variation was assumed to be zero as this data is unavailable. The calculated electric fields closely represent the resultant fields at the actual surface due to the physical roughness, chemical roughness and the accelerating gradient. Electrons with zero initial velocity were launched from various points on the surface. Their motion was tracked in the calculated electric fields until a point sufficiently far away from the surface where the roughness-induced transverse fields become negligible. The rms of the transverse velocities gained by these electrons was used to estimate the roughness-induced MTE increase. The details of this calculation are provided elsewhere [Gevorkyan *et al.* (2018)].

Fig. 2.4 shows this calculated roughness-induced MTE for the 3 surfaces measured at various accelerating gradients. For the film of Si, the roughness induced MTE starts from near 0 at very low electric fields and increases rapidly at larger gradients. At 100 MV/m (typically the maximum accelerating gradient used in photoinjectors) the roughness induced MTE is 40 meV (ΔMTE$/E = 0.4$ meV/(MV/m)). The zero roughness induced
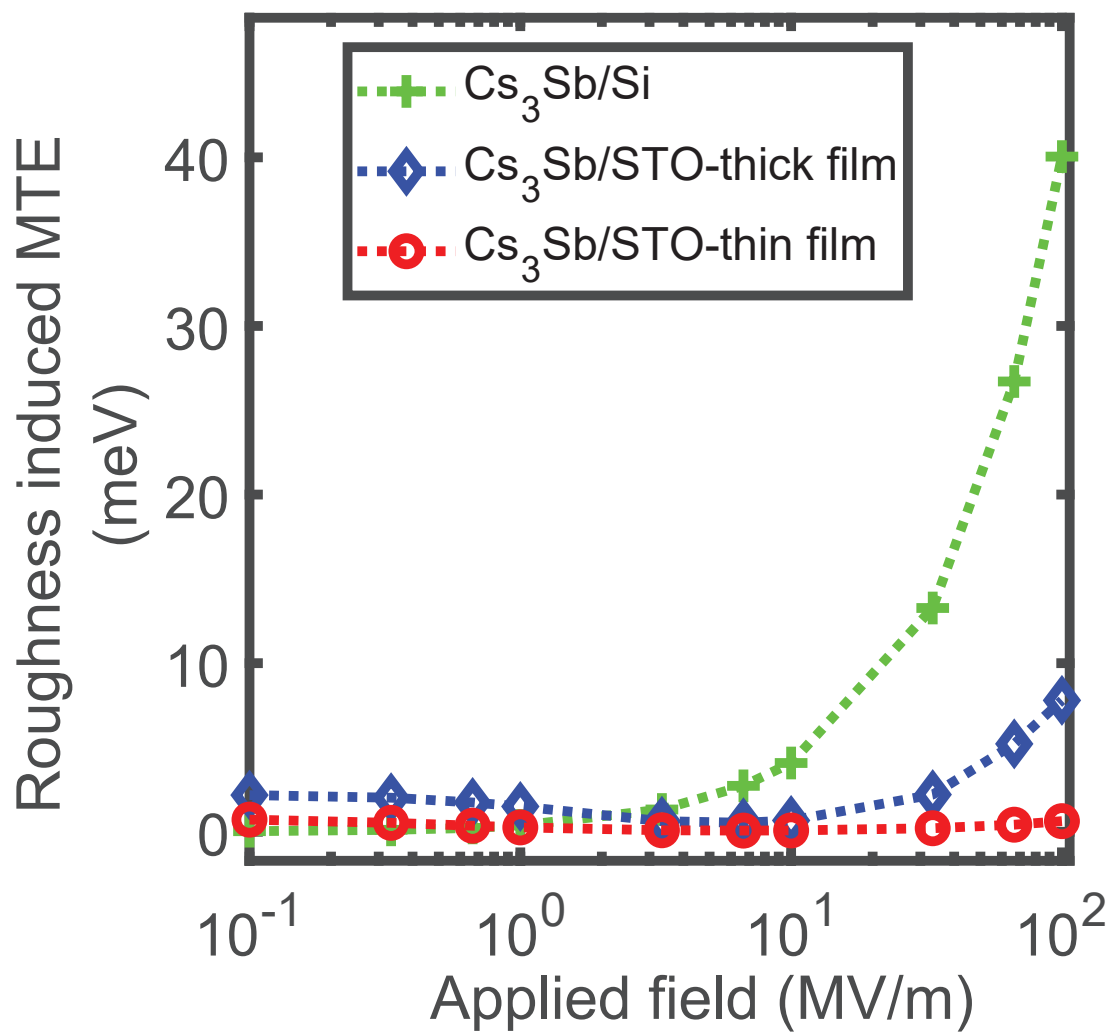
Figure 2.4: Effect of Surface Roughness on MTE. The Calculations For the Film on Si Include Effects of Physical Roughness Only.

MTE at low fields is due to the uniform surface potential assumption for the films on Si. In reality, we expect the low-accelerating-gradient-roughness-induced MTE to be larger due to variations in the surface potential (chemical roughness). The MTE increase calculations performed for the films on STO include effects of both physical and chemical roughness. The thick film on STO is significantly smoother giving an MTE increase of only 8 meV at 100 MV/m (dominated by physical roughness) and only 2.2 meV at low gradients (dominated by chemical roughness). Finally, the thin film on STO is smoothest and gives roughness induced MTE smaller than 1 meV at all gradients.

2.5 Conclusion

In conclusion, we have demonstrated the growth of high QE, topographically ultra-smooth and chemically homogeneous Cs_3Sb cathodes on lattice-matched STO substrates. Our results show that the films grown on STO exhibit sufficiently small physical and chemical roughness to make the roughness induced MTE increase inconsequential at all commonly-used field gradients in photoinjectors.

2.6 Acknowledgements

2.7 References

"Cs-pellets", https://www.saesgetters.com/ (2023).

"Effusion cells", https://www.mbe-komponenten.de/products/mbe-components/effusion-cells.php/ (2023).

"Sb pellets", https://www.alfa.com/en/ (2023).

"Sto substrates", https://www.mtixtl.com/ (2023).

Bae, J., I. Bazarov, L. Cultrera, J. Maxson, P. Musumeci, X. Shen, S. Karkare and H. Padmore, "Multi-photon photoemission and ultrafast electron heating in cu photocathodes at threshold", TUPML026 (2018).

Cultrera, L., S. Karkare, H. Lee, X. Liu, I. Bazarov and B. Dunham, "Cold electron beams from cryocooled, alkali antimonide photocathodes", Physical Review Special Topics-Accelerators and Beams **18**, 11, 113401 (2015).

Dowell, D. H. and J. F. Schmerge, "Quantum efficiency and thermal emittance of metal photocathodes", Phys. Rev. ST Accel. Beams. **12**, 074201 (2009).

Dunham, B., J. Barley, A. Bartnik, I. Bazarov, L. Cultrera, J. Dobbins, G. Hoffstaetter, B. Johnson, R. Kaplan, S. Karkare *et al.*, "Record high-average current from a high-brightness photoinjector", Applied Physics Letters **102**, 3, 034105 (2013).

Feng, J., S. Karkare, J. Nasiatka, S. Schubert, J. Smedley and H. Padmore, "Near atomically smooth alkali antimonide photocathode thin films", Journal of Applied Physics **121**, 4, 044904 (2017).

Feng, J., J. Nasiatka, W. Wan, S. Karkare, J. Smedley and H. A. Padmore, "Thermal limit to the intrinsic emittance from metal photocathodes", Applied Physics Letters **107**, 13, 134101 (2015).

Ferrario, M., "Overview of fel injectors, 2015", Proc.of EPAC, Edinburgh, Scotland (2015).

Gevorkyan, G. S., S. Karkare, S. Emamian, I. V. Bazarov and H. A. Padmore, "Effects of physical and chemical surface roughness on the brightness of electron beams from photocathodes", Phys. Rev. Accel. Beams. **21**, 093401 (2018).

Gordon, M., S. B. van der Geer, J. M. Maxson and Y. K. Kim, "Point-to-point coulomb effects in high brightness photoelectron beam lines for ultrafast electron diffraction", Phys. Rev. Accel. Beams. **24**, 084202 (2021).

Hagino, M. and T. Takahashi, "Thickness of cs-sb films relative to the original sb films", J. Appl. Phys. **37**, 10 (1966).

Karkare, S., G. Adhikari, W. A. Schroeder, J. K. Nangoi, T. Arias, J. Maxson and H. Padmore, "Ultracold electrons via near-threshold photoemission from single-crystal cu (100)", Physical review letters **125**, 5, 054801 (2020).

Karkare, S. and I. Bazarov, "Effects of surface nonuniformities on the mean transverse energy from photocathodes", Physical Review Applied **4**, 2, 024015 (2015).

Knill, C. J., H. A. Padmore and S. Karkare, "Near-threshold nonlinear photoemission from cu(100)", Proceedings of the 9th International Particle Accelerator Conference, (2021) paper WEPAB099 (2021).

Mathew, K., A. K. Singh, J. J. Gabriel, K. Choudhary, S. B. Sinnott, A. V. Davydov, F. Tavazza and R. G. Hennig, "Mpinterfaces: A materials project based python tool for high-throughput computational screening of interfacial systems", Comput. Mater. Sci. **122**, 183 (2016).

Maxson, J., P. Musumeci, L. Cultrera, S. Karkare and H. Padmore, "Ultrafast laser pulse heating of metallic photocathodes and its contribution to intrinsic emittance", Nuclear Instruments and Methods in Physics Research Section A: Accelerators, Spectrometers, Detectors and Associated Equipment **865**, 99–104 (2017).

Maxson, J. M., I. V. Bazarov, W. Wan, H. A. Padmore and C. E. Coleman-Smith, "Fundamental photoemission brightness limit from disorder induced heating", Phys. Rev. Accel. Beams. **15**, 103024 (2013).

Melitz, W., J. Shena, A. C. Kummel and S. Lee, "Kelvin probe force microscopy and its application", Surface Science Reports **66** (2011).

Musumeci, P., J. G. Navarro, J. Rosenzweig, L. Cultrera, I. Bazarov, J. Maxson, S. Karkare and H. Padmore, "Advances in bright electron sources", Nuclear Instruments and Methods in Physics Research Section A: Accelerators, Spectrometers, Detectors and Associated Equipment **907**, 209–220 (2018).

Oudheusden, T. V., E. F. de Jong, S. B. van der Geer, W. O. 't Root, O. J. Luiten and B. J. Siwick, "Electron source concept for single-shot sub-100 fs electron diffraction in the 100 kev range", J. Appl. Phys. **102**, 093501 (2007).

Parzyck, C., A. Galdi, J. Nangoi, W. DeBenedetti, J. Balajka, B. Faeth, H. Paik, C. Hu, T. Arias, M. Hines *et al.*, "Single-crystal alkali antimonide photocathodes: High efficiency in the ultrathin limit", Physical Review Letters **128**, 11, 114801 (2022).

Paul, J. T., A. Galdi, C. Parzyck, K. M. Shen, J. M. Maxson and R. G. Hennig, "Computational synthesis of substrates by crystal cleavage", NPJ Comput. Mater. **7** (2021).

Rosenzweig, J., N. Majernik, R. Robles, G. Andonian, O. Camacho, A. Fukasawa, A. Kogar, G. Lawler, J. Miao, P. Musumeci *et al.*, "An ultra-compact x-ray free-electron laser", New Journal of Physics **22**, 9, 093067 (2020).

Saha, P., O. Chubenko, G. S. Gevorkyan, A. Kachwala, C. J. Knill, C. Sarabia-Cardenas, E. Montgomery, S. Poddar, J. T. Paul, R. G. Hennig *et al.*, "Physically and chemically smooth cesium-antimonide photocathodes on single crystal strontium titanate substrates", Applied Physics Letters **120**, 19, 194102 (2022).

Schmeißer, M. A. H., S. Mistry, H. Kirschner, S. Schubert, A. Jankowiak, T.Kamps and J. Kuhn, "Towards the operation of cs-k-sb photocathodes in superconducting rf photoinjectors", Phys. Rev. Accel. Beams. **21**, 113401 (2018).

Schubert, S., M. Ruiz-Oses, I. Ben-Zvi, T. Kamps, X. Liang, E. Muller, K. Mueller, H. A. Padmore, T. Rao, X. Tong, T. Vecchione and J. Smedley, "Bi-alkali antimonide photocathodes for high brightness accelerators", Appl. Materials **1**, 032119 (2013).

Vecchione, T., I. Ben-Zvi, D. H. Dowell, J. Feng, T. Rao, J. Smedley, W. Wan and H. A. Padmore, "A low emittance and high efficiency visible light photocathode for high brightness accelerator-based x-ray light sources", Appl. Phys. Lett. **99**, 034103 (2011).

Vecchione, T., D. Dowell, W. Wan, J. Feng and H. Padmore, "Quantum efficiency and transverse momentum from metals", Proceedings of FEL 2013, New York, NY (2013).

Chapter 3

THEORY OF PHOTOEMISSION FROM CATHODES WITH DISORDERED SURFACES

This chapter was originally published as Ref. Saha *et al.* (2023).

3.1   Abstract

Linear-accelerator- based applications like X-ray Free Electron Lasers (XFEL), Ultrafast Electron Diffraction (UED), electron beam cooling and Energy Recovery Linacs (ERL) use photoemission-based cathodes in photoinjectors for electron sources. Most of these photocathodes are typically grown as polycrystalline materials with disordered surfaces. In order to understand the mechanism of photoemission from such cathodes and completely exploit their photoemissive properties, it is important to develop a photoemission formalism that properly describes subtleties of these cathodes. The Dowell-Schmerge (D-S) model often used to describe the properties of such cathodes gives the correct trends for photoemission properties like the quantum efficiency (QE) and the mean transverse energy (MTE) for metals, however, it is based on several unphysical assumptions. In the present work, we use the Spicer's three-step photoemission formalism to develop a photoemission model that results in the same trends for QE and MTE as the D-S model without the need for any unphysical assumptions and is applicable to defective thin-film semiconductor cathodes along with metal cathodes. As an example, we apply our model to Cs_3Sb thin films and show that their near-threshold QE and MTE performance is largely explained by the exponentially decaying defect density of states near the valance band maximum.

3.2 Introduction

The development of advanced accelerator applications such as X-ray Free Electron Lasers (XFEL) [Rosenzweig *et al.* (2020)], Energy Recovery Linacs (ERL) [Gruner *et al.* (2002)] and Ultrafast Electron Diffraction (UED) [Oudheusden *et al.* (2007)] depends to a large extent on the brightness of electron sources used to generate electron bunches. High density bunched electron beams for such applications are typically produced using photoinjectors, which consist of a photocathode placed in an accelerating electric field $\mathscr{E}$ along with electron optics to mitigate the brightness-degrading effects of space charge.

Electron beam brightness is a key figure of merit for these applications. The maximum charge density that can be extracted from a photoinjector is proportional to the nth power of the accelerating electric field $\mathscr{E}$. Hence the maximum brightness achievable from a photoinjector is proportional to the nth exponent of the electric field $\mathscr{E}$ and is inversely proportional to the Mean Transverse Energy (MTE) of the photoemitted electrons [Musumeci *et al.* (2018)]

$$B \propto \frac{\mathscr{E}^n}{\text{MTE}}, \tag{3.1}$$

where *n* is a real number between 1 and 2, depending on the design of a photoinjector. The MTE is related to the intrinsic emittance ε_i, which is a measure of the volume occupied by the beam in phase space, via the following expression

$$\varepsilon_i = \sigma_x \sqrt{\frac{\text{MTE}}{mc^2}}, \tag{3.2}$$

where σ_x is the rms transverse beam size, *m* is the rest mass of a free electron and *c* is the speed of light.

The maximum possible accelerating field depends on the design of the photoinjector, but the MTE is a property of the cathode material, its surface as well as laser driving

conditions. It is imperative to reduce the MTE in order to maximize the beam brightness. The MTE is often lowered by operating the cathode near its photoemission threshold, at the cost of its Quantum Efficiency (QE) [Feng *et al.* (2015)]. MTE and QE, which are two intrinsic properties of the photocathode, can potentially limit the beam brightness and are studied in order to understand the photoemission process.

The Dowell-Schmerge (D-S) scheme [Dowell *et al.* (2006); Dowell and Schmerge (2009)], which is based on the Sommerfeld's free electron gas theory in solids, coupled with Spicer's three-step model [Spicer (1958)] is often used to explain photoemission from most cathodes in use today. Under the assumptions of nearly free electron gas model, parabolic dispersion relations, conservation of transverse momentum, constant density of states and zero lattice temperature [Dowell *et al.* (2006); Dowell and Schmerge (2009)], the expressions for QE and MTE were analytically calculated by D-S.

In the D-S scheme, the QE was shown to vary quadratically with the excess energy E_{excess} as

$$QE \propto E_{excess}^2, \tag{3.3}$$

where the excess energy is defined as the difference between the incident photon energy $\hbar\omega$ and the effective material work function ϕ, after accounting for the Schottky reduction [Kiziroglou *et al.* (2008)]. Well above the photoemission threshold, i.e. at large excess energies, the MTE was found to vary linearly with the excess energy as

$$MTE = \frac{E_{excess}}{3}. \tag{3.4}$$

A wide range of polycrystalline photocathodes like Sb [Dowell and Schmerge (2009); Feng *et al.* (2015)], Cu [Dowell and Schmerge (2009); Karkare *et al.* (2020)], Cs_2Te [Pierce *et al.* (2021)], and alkali-antimonides like Cs_3Sb [Cultrera *et al.* (2011)] and Na_2KSb [Cul-

29

trera *et al.* (2016)] have demonstrated MTE proportional to one-third of the excess energies at large excess energies, as predicted by the D-S scheme.

A more recent work by Vecchione *et al.* (2013), often referred to as the extended D-S scheme, has included the effect of non-zero temperature on the Fermi-Dirac distribution of electrons, which leads to the polylogarithmic expressions for QE and MTE

$$\text{QE} = S\text{Li}_2[-\exp(E_{excess})], \tag{3.5}$$

$$\text{MTE} = k_B T \frac{\text{Li}_3[-\exp(E_{excess})]}{\text{Li}_2[-\exp(E_{excess})]}, \tag{3.6}$$

where k_B is the Boltzmann constant, Li_2 and Li_3 are the polylogarithm functions of order 2 and 3 respectively, S is a constant and T is the temperature of the electrons in the crystal. For smaller laser fluences, T is the lattice temperature as the electrons can be considered to be in equilibrium with the lattice. Near the photoemission threshold, where the excess energies are practically zero or negative, emission essentially occurs from the Fermi tail, which limits the value of MTE to the thermal limit of $k_B T$. The thermal limit for MTE has been experimentally demonstrated from thin polycrystalline Sb films at room temperature [Feng *et al.* (2015)] and Cu (100) cathodes at cryogenic temperatures [Karkare *et al.* (2020)].

A large number of assumptions [Dowell *et al.* (2006)] have been considered in the D-S scheme, which do not hold true for the aforementioned cathodes with disordered surfaces. For example, the transverse momentum is not a conserved quantity for polycrystalline cathodes with disordered surfaces [Hüfner (2003)]. For semiconductor cathodes, the valence density of states close to the Fermi level, from which photoexcitation takes place near the threshold, cannot be assumed to be a constant. Also, parabolic dispersion relations are not obeyed by band structures of most cathodes, especially near the vacuum level. Thus, the

assumptions mentioned above, which are intrinsic to the D-S scheme, cannot be applied to many of the cathodes that have been experimentally studied. Nonetheless, all of the cathodes mentioned earlier have experimentally demonstrated QE and MTE near and above the threshold, as predicted by the D-S scheme.

The D-S scheme, through the unphysical assumptions of the single-band-parabolic dispersion relation and the conservation of transverse momentum, happens to arrive at a distribution of emitted electrons in which parabolic dispersion relationship of the emitted (free) electrons is uniformly filled, giving the QE and MTE relationships. We realized that such a uniformly filled dispersion relation is also possible due to a disordered surface – which is the case for all photocathodes used in guns thus far. An atomically disordered surface can cause electrons to be scattered uniformly in all energetically allowed momenta.

In this paper, within the framework of Spicer's three-step formulation [Spicer (1958)], we develop a photoemission model, which reproduces expressions for QE and MTE that were obtained by the D-S scheme, without resorting to the unrealistic assumptions. The first two steps of optical excitation and electron transport have been treated in the traditional way as in the D-S scheme. The third step of emission has been treated in an unconventional manner by incorporating the quantum mechanical effect of scattering from a disordered surface. Section 2 describes the three steps of our photoemission model in detail. We then apply this model to Cs_3Sb cathodes in Section 3 and show how QE and MTE near and below the threshold can be dominated by defect/impurity density of states lying within the band gap of Cs_3Sb cathodes.

3.3 Formulation of the Photoemission Model

In this section, we discuss the three steps of photoemission: optical excitation, transport and emission in detail and show how we can derive the expressions for QE and MTE from cathodes with disordered surfaces.

31
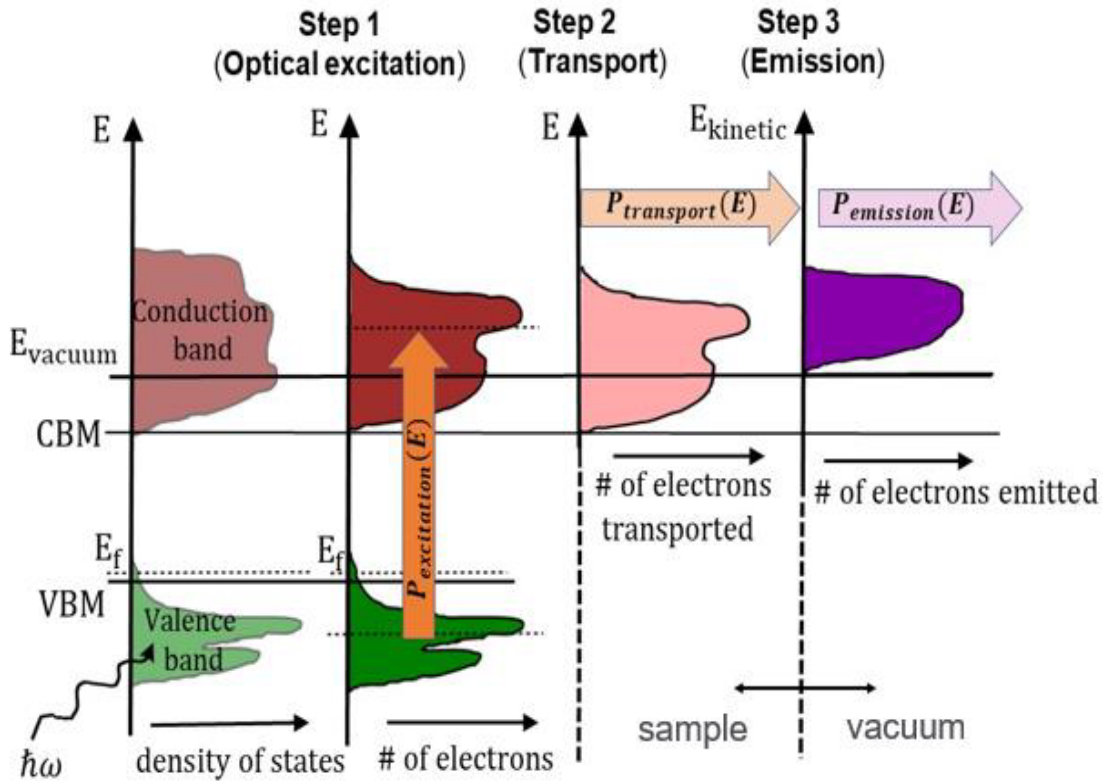
Figure 3.1: Schematic of the Photoemission Model, Showing the Three Steps of Optical Excitation, Transport And Emission of Electrons into Vacuum. The above Figure Represents a Density of States with a Band Gap Corresponding to That of a Semiconductor, but the Model Presented Here Is Equally Applicable to Metals With Disordered Surfaces. VBM and CBM Stand for Valence Band Maximum and Conduction Band Minimum, Respectively.

3.3.1 Excitation

The first step is the optical excitation of electrons from the occupied valence band density of states (DOS) into the vacant conduction band DOS due to the absorption of photons with energy $\hbar\omega$ as indicated by Step 1 in Fig. 3.1. The probability for this transition to occur from the state with energy E, measured with respect to the Fermi level energy, to $E+\hbar\omega$ follows from Bergund and Spicer's formalism Bergund and Spicer (1964). For polycrystalline cathodes in which the band structure is not well-defined, the probability is proportional to the number of electrons in the occupied states at energy E, which is given by

the product term $D(E)f(E)$, and the number of unoccupied states at energy $E+\hbar\omega$, which is similarly given by $D(E + \hbar\omega)[1\text{-}f(E+\hbar\omega)]$. Here, $D(E)$ denotes the density of states at initial energy of the electrons E, similarly $D(E + \hbar\omega)$ represents the density of states at energy $E+\hbar\omega$. Here, $f(E)$ is the Fermi-Dirac distribution which is used to define the occupation probability of the electrons

$$f(E) = \frac{1}{[1 + \exp(\frac{E - E_f}{k_B T})]}, \tag{3.7}$$

where E_f is the position of Fermi level. The probability of excitation to occur can be written as

$$P_{excitation}(E) \propto D(E)f(E)D(E + \hbar\omega)[1 - f(E + \hbar\omega)]. \tag{3.8}$$

For single crystalline cathodes, excitation can be modeled using vertical transitions in the band structure, obeying the law of conservation of energy and momentum [Hüfner (2003)]. However, we do not consider the single crystalline case in this paper.

3.3.2 Transport

The second step is the transport of these photoexcited electrons to the cathode-vacuum interface. In the case of metallic cathodes, electron-electron (e-e) scattering is the most dominant scattering mechanism during transport. When such scattering events occur, the electrons excited within few 100 meV above the threshold lose enough energy that they fall below the vacuum level and do not get emitted at all. For photon energies within few 100 meV of the threshold, the fraction of electrons that are lost due to such an e-e scattering process can be treated as a constant invariant of the photon energy and electron energy [Spicer and HerreraGómez (1993)].

In the case of semiconductor cathodes with a low electron affinity, the e-e scattering is prohibited due to lack of final states into which scattered electrons can relax, owing to the presence of the forbidden band gap energy [Spicer and HerreraGómez (1993)].This

makes electron-phonon/electron-plasmon/electron-impurity (e-p/e-i) scattering processes dominant in semiconductor materials [Karkare *et al.* (2013); Gupta *et al.* (2017); Chubenko *et al.* (2021)]. The energy distribution of the electrons, which reach the interface, gets modified due to these scattering processes. However, given the small thickness of these cathodes and low energy transfer rates, a relatively large fraction of the scattered electrons retain enough energy to still get emitted, resulting in a higher overall QE compared to metallic cathodes. The losses suffered due to these scatterings and the resulting change in the electron energy distribution during transport can be studied in greater detail by employing the Monte Carlo techniques to solve the Boltzmann transport equation [Karkare *et al.* (2013); Gupta *et al.* (2017); Chubenko *et al.* (2021)]. If the cathode thickness is smaller than the mean free path of excited electrons (typically in the range of several 10s to 100s of nm for semiconductors), the number of scattering events before emission can be assumed to be very small such that it will not affect the energy distribution dramatically. In such situations we can assume that the probability of an excited electron reaching the surface is invariant with the electron and photon energy.

In this paper, we assume that the cathodes are either metallic of semiconducting thin films with thickness smaller than the mean free path of the electrons. Thus, the energy distribution of the excited electrons does not undergo any significant changes during transport. Hence the probability of an excited electron reaching the surface with enough energy for emission can be accounted for by a constant, invariant of the photon energy and the electron energy. This probability has been denoted by a constant C_t at all photon energies

$$P_{transport}(E) = C_t. \tag{3.9}$$

3.3.3 Emission

The third step is the emission of electrons at the cathode-vacuum interface into vacuum by overcoming the workfunction/ photoemission threshold of the material. Here we

make the assumption that an electron, incoming towards the surface with any wave vector, scatters uniformly into all energetically possible wave vectors with equal probability. This assumption can be justified due to a quantum mechanical scattering effect of the electrons from a disordered surface.

Consider a surface with a disorder in the form of a very small sinusoidal variation in height or work function with a period comparable to that of the de Broglie wavelength of the emitted electrons. For emitted electrons with kinetic energies in the 1 meV-1 eV range which is typical for near threshold emisison from photocathodes, the de Broglie wavelength is around 1-40 nm. Electrons, scattering quantum mechanically from such a surface, can scatter into a transverse wave vector equal to the transverse (parallel to the surface) part of incoming electron wave vector plus harmonics of the wave-vector of the periodic disorder on the surface, so long as it is energetically allowed [Karkare and Bazarov (2015)]. Extending this approach to a randomly disordered surface which is composed of all wave vectors, one can envision that any incoming electron wave vector will be scattered into all energetically allowed transverse wave vectors with equal probability, justifying our assumption.

The conservation of energy imposes an upper limit on the values of transverse momentum $k_\perp$, with which the electrons can be emitted. The maximum transverse momentum $k_{\perp max}$ is given by the kinetic energy $E_{kinetic}$ as

$$k_{\perp max} = \sqrt{\frac{2mE_{kinetic}}{\hbar^2}}, \tag{3.10}$$

where $\hbar$ is the reduced Planck's constant. The emission probability of electrons with a particular energy E is then proportional to the number of vacuum states it can scatter into and can be expressed as

$$P_{emission}(E) \propto \int_0^{k_{\perp max}} 2\pi k_\perp dk_\perp = C_e E_{kinetic}, \tag{3.11}$$

35

where $E_{kinetic} = E + \hbar\omega - E_{vacuum}$ is the kinetic energy of the electrons and E_{vacuum} is the vacuum level position of the cathode material measured with respect to the valence band maximum (VBM) and C_e is a constant that involves the 2D density of states (for the two transverse directions) and will have units of 1/energy.

The variation of the workfunction being considered here is on a spatial scale smaller than or comparable to the de-Broglie wavelength of the emitted electrons. Hence, we do not expect this variation to cause significant spatial non-uniformity in the emitted current, unlike in the case where the work function variation is on the larger micron spatial scales [Jensen *et al.* (2008)]. In our case, we can assume the workfunction to have a constant average value and account for the variation only in the surface scattering of the electrons during emission.

The emission probability of the electrons, which reach the cathode-vacuum interface, is thus proportional to their kinetic energy. This is indicated by Step 3 in Fig. 3.1. This also implies that only those electrons, which have kinetic energies greater than the vacuum level energy, will get emitted.

Combining the probabilities for excitation, transport and emission to occur as discussed above, the expression for the number of electrons emitted can be written as

$$\#e^- \text{emitted} = \int_{-\infty}^{\infty} P_{excitation}(E)P_{transport}(E)P_{emission}(E)dE. \tag{3.12}$$

Similarly, the number of electrons excited is given by

$$\#e^- \text{excited} = \int_{-\infty}^{\infty} P_{excitation}(E)dE. \tag{3.13}$$

Quantum efficiency can be defined as the ratio of the number of electrons emitted to the number of electrons excited

$$QE = \alpha \frac{\#e^- \text{emitted}}{\#e^- \text{excited}}, \tag{3.14}$$

where α accounts for optical absorption by the cathode.

Using Equations 3.8 through 3.14, expression for the QE as a function of the photon energy can be written as

$$\text{QE}(\hbar\omega) = \alpha C_t C_e \frac{\int_{-\infty}^{\infty} D(E) f(E) D(E+\hbar\omega)[1 - f(E+\hbar\omega)] E_{kinetic} dE}{\int_{-\infty}^{\infty} D(E) f(E) D(E+\hbar\omega)[1 - f(E+\hbar\omega)] dE}. \tag{3.15}$$

Similarly, the expression for MTE can be formulated by calculating the average transverse momenta squared

$$\text{MTE}(\hbar\omega) = \frac{\hbar^2}{2m} \frac{\int_{-\infty}^{\infty} D(E) f(E) D(E+\hbar\omega)[1 - f(E+\hbar\omega)] dE \int_0^{k_{\perp max}} 2\pi k_\perp k_\perp^2 dk_\perp}{\int_{-\infty}^{\infty} D(E) f(E) D(E+\hbar\omega)[1 - f(E+\hbar\omega)] dE \int_0^{k_{\perp max}} 2\pi k_\perp dk_\perp}, \tag{3.16}$$

which, by substituting the value of $k_{\perp max}$ from Equation 3.10, reduces to

$$\text{MTE}(\hbar\omega) = (1/2) \frac{\int_{-\infty}^{\infty} D(E) f(E) D(E+\hbar\omega)[1 - f(E+\hbar\omega)] E_{kinetic}^2 dE}{\int_{-\infty}^{\infty} D(E) f(E) D(E+\hbar\omega)[1 - f(E+\hbar\omega)] E_{kinetic} dE}. \tag{3.17}$$

We first consider a constant density of states and finite lattice temperature in order to compare our simulations for QE and MTE to the extended D-S scheme. To begin with, we solve the expressions for QE and MTE in Equations 3.15 and 3.17 analytically in the following manner. Under the assumption of a constant DOS, Equation 3.15 reduces to

$$\text{QE}(\hbar\omega) \propto \frac{\int_{-\infty}^{\infty} f(E)[1 - f(E+\hbar\omega)](E+\hbar\omega - E_{vacuum}) dE}{\int_{-\infty}^{\infty} f(E)[1 - f(E+\hbar\omega)] dE}. \tag{3.18}$$

At zero temperature, Equation 3.18 gives

$$\text{QE}(\hbar\omega) \propto \frac{\int_{E_{vacuum}-\hbar\omega}^{0} (E+\hbar\omega - E_{vacuum}) dE}{\int_{-\hbar\omega}^{0} dE}. \tag{3.19}$$

Equation 3.19 can be integrated to obtain the well-known dependence of QE on excess energy as predicted by the D-S scheme

$$\text{QE}(\hbar\omega) \propto (\hbar\omega - E_{vacuum})^2. \tag{3.20}$$

The excess energy is defined as the difference between the incident photon energy and the work function of the material. Typically, work function is defined as the vacuum level

energy with respect to the Fermi level. In the case of semiconductor photocathodes, the Fermi level is not too well-defined as it often lies within the forbidden band gap. Hence, it is reasonable to modify the expression of work function to be the difference in energy between the vacuum level and the highest occupied electron level, which in this case is the VBM instead of Fermi level. Therefore for semiconductor cathodes, the excess energy can be defined as the difference in energy between the incident photon energy and the vacuum level energy. The VBM is considered to be the zero level for reference.

Under the same assumption of a constant DOS, expression for MTE in Equation 3.17 reduces to

$$\text{MTE}(\hbar\omega) \propto \frac{1}{2} \frac{\int_{-\infty}^{\infty} f(E)[1 - f(E + \hbar\omega)](E + \hbar\omega - E_{vacuum})^2 dE}{\int_{-\infty}^{\infty} f(E)[1 - f(E + \hbar\omega)](E + \hbar\omega - E_{vacuum}) dE}. \tag{3.21}$$

Assuming a zero temperature dependence, Equation 3.21 reduces to

$$\text{MTE}(\hbar\omega) \propto \frac{1}{2} \frac{\int_{E_{vacuum} - \hbar\omega}^{0} (E + \hbar\omega - E_{vacuum})^2 dE}{\int_{-\hbar\omega}^{0} (E + \hbar\omega - E_{vacuum}) dE}. \tag{3.22}$$

Integrating Equation 3.22 results in MTE being proportional to one-third the excess energy obtained by the D-S scheme

$$\text{MTE}(\hbar\omega) = \frac{(\hbar\omega - E_{vacuum})}{3}. \tag{3.23}$$

Equations 3.18 and 3.21 can be numerically integrated to obtain the spectral response of QE and MTE under the assumption of a constant DOS for non-zero temperatures. This has been plotted in Fig. 3.2 and Fig. 3.3, respectively. We see in Fig. 3.2 that QE varies as square of the excess energy as was predicted by the D-S scheme. MTE varies linearly with the excess energy as $E_{excess}/3$ beyond threshold and goes down to $k_B T$ at zero/ negative excess energies as shown in Fig. 3.3.

Thus, our photoemission model reproduces the same experimentally measured QE and MTE expressions as the D-S scheme without the use of unphysical assumptions like
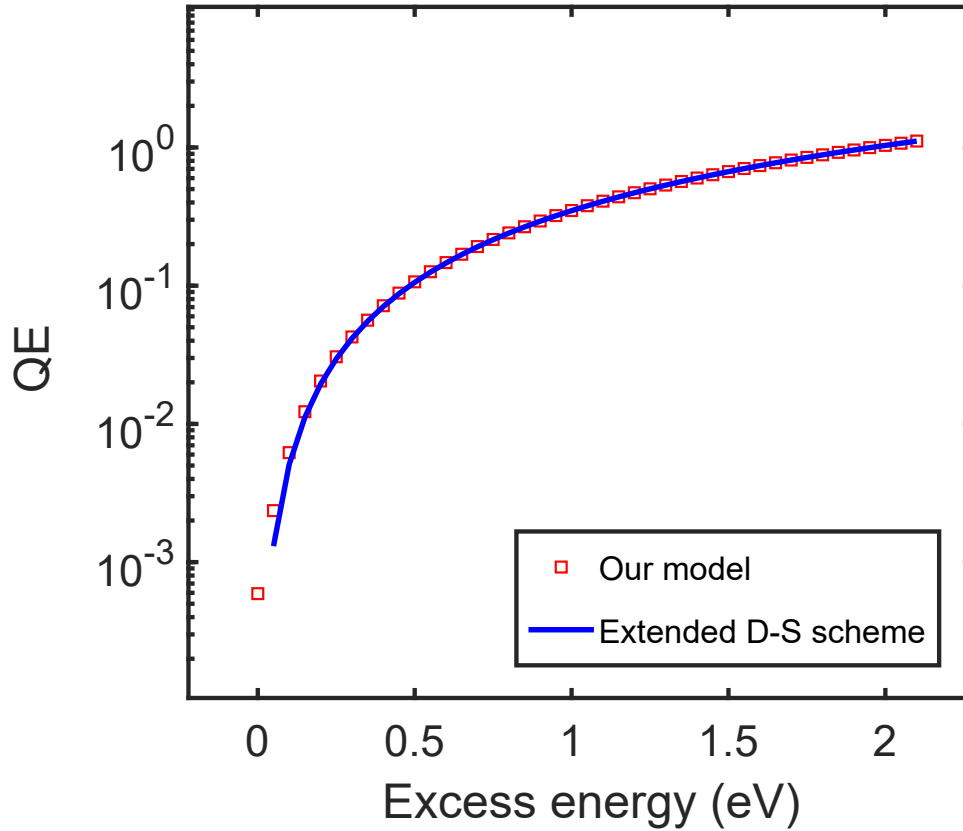
Figure 3.2: Quantum Efficiency as a Function of the Excess Energy, Assuming a Constant Density of States, Is Calculated using Our Model (Equation 3.18). The Spectral Response of QE, Calculated Using the Extended D-S Scheme Under the Same Assumption (Equation 3.5), is Included for Comparison. The Only Relevant Parameter Is the Temperature. The QE Was Normalized to 1.0 at 2.0 eV Excess Energy.

parabolic dispersion relations and conservation of transverse momentum for disordered surfaces. Furthermore, our model can easily be extended to explain near the threshold photoemission from in-gap defect states in semiconductor cathodes. In the next section, we use this model to show that the experimentally measured MTE from alkali-antimonide semiconductor cathodes can be limited by such defect states.
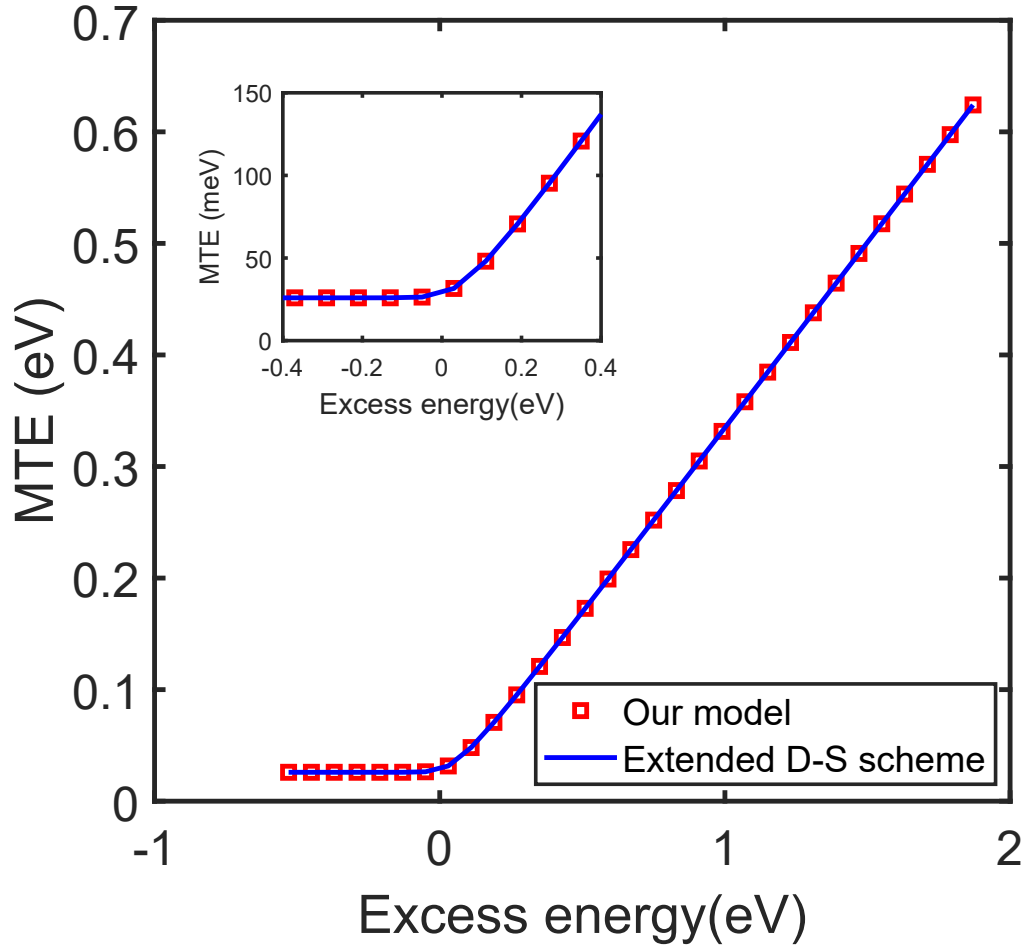
Figure 3.3: Mean Transverse Energy as a Function of the Excess Energy under the Assumption of a Constant Density of States Is Calculated Using Our Model (Equation 3.21). The Spectral Response of MTE Calculated Using the Extended D-S Scheme (Equation 3.6) under the Same Assumption, Is Included for Comparison. The Inset Shows the near Threshold MTE Values Calculated Using Our Model and the Extended D-s Scheme, For Comparison.

3.4   Application to Cesium-antimonide photocathodes

High QE photocathodes like Cs_3Sb are an excellent choice for electron sources in different high beam brightness applications. Due to their high QE, large laser power does not have to be used to extract the required charge densities, thereby significantly mitigating the possibility of MTE growth via different non-linear effects [Maxson *et al.* (2017); Bae *et al.* (2018)].

In an attempt towards maximizing brightness by reducing MTE, the MTE from Cs_3Sb photocathodes close to the threshold has been measured at both room and cryogenic temperatures. At both temperatures, MTE did not go all the way down to the thermal limit k_BT as was predicted by the extended D-S scheme. It was measured to be 40 meV at room temperature and 22 meV at 90 K - significantly larger than k_BT, which is 25 meV and 8 meV at room temperature and 90 K, respectively [Cultrera *et al.* (2015)]. This discrepancy was attributed to the surface roughness and work function variations [Cultrera *et al.* (2015)], and defect states within the band gap [Spicer (1958)]. While effects of the surface roughness and work function variations on MTE have been quantitatively investigated in great detail [Feng *et al.* (2017); Karkare and Bazarov (2015); Gevorkyan *et al.* (2018)], the effect of in-gap defect states on QE and MTE has never been investigated. In this section, we apply our photoemission model to investigate the effect of the defect states on QE and MTE and show how larger MTE could arise from the in-gap defect states.

In our model, we use the valence and conduction band DOS of Cs_3Sb calculated from the density functional theory (DFT) [Nangoi *et al.* (2022)]. The DFT calculations have been performed, assuming that these cathodes are single crystalline. In order to account for the polycrystalline and disordered nature of these cathodes, an exponential tail of width 0.04 eV has been added to the valence band DOS. This tail width has been used to obtain the best possible fit with experimental data. Such a value is also typical for exponential tail

width of disordered semiconductors [Gupta *et al.* (2017); Sa-yakanit and Glyde (1987)].
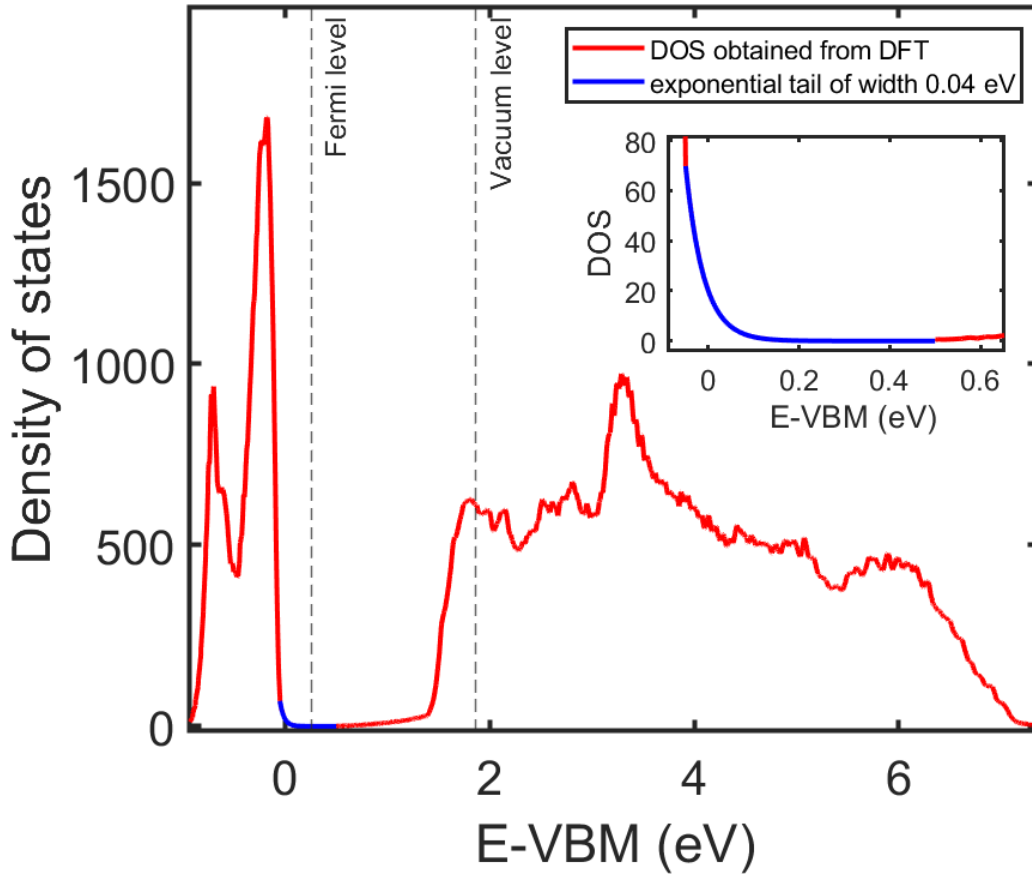
Figure 3.4: Density of States of Cs$_3$sb Cathodes with In-gap Defect States as Indicated by the Exponential Tail of Width 0.04 eV (Marked in Blue). The Approximate Position of the Fermi Level and Vacuum Level, Which Have Been Used in the Simulation, Are Indicated by Dotted Lines. A Blowup of the Dos for Defect States Is Provided as an Inset.

Fig. 3.4 shows the density of states that has been used to model photoemission from Cs$_3$Sb cathodes. The approximate position of the Fermi level E_f and the vacuum level E_{vacuum}, which have been used in the simulation, are indicated by dotted lines in Fig. 3.4. Table 3.1 gives the values of these two material-dependent parameters, which have been used in the simulation of QE and MTE. These values have been used as they provide the best fit to the QE experimental data. A variation of 0.1-0.2 eV in the position of the Fermi level is common amongst semiconductors over a temperature range between 20-300 K

[Nguyena and O'Leary (2000)]. All energies are measured with respect to the VBM.

T(K)	E_f (eV)	E_{vacuum} (eV)
300	0.26	1.86
90	0.12	1.95
77	0.1	1.95

Table 3.1: Simulation Parameters and Their Values. These Values Have Been Because They Provide the Best Fit to the QE Experimental Data. A Positive Value of E_F, Which Is Less than Half the Band Gap, Indicates a P-doped Film.

The spectral response of QE from Cs_3Sb cathodes is calculated using Equation 3.15. Fig. 3.5 shows a close resemblance of the calculated values of QE with experimental values at two sets of temperature: room temperature 300 K [Saha *et al.* (2022)] and cryogenic temperature 77 K [Spicer (1958)]. The photoemission threshold is marked by the knee around ~ 2 eV. Below the threshold, the QE drops sharply. Without the presence of defect states, the QE should drop to zero right at the threshold. However, the exponentially decaying tail in QE below the threshold is due to the defect density of states, which decreases exponentially with increasing energy. It is also affected by the location of the Fermi level to some extent.

A reduction in the QE is observed when the cathode is cooled down to 77 K [Spicer (1958)]. This is explained by the shorter Fermi tail leading to the reduction in a number of defect states filled with electrons, with energies enough to be excited above the threshold.

Fig. 3.6 shows the behavior of calculated MTE values at large excess energies (using Equation 3.17) compared with experimentally obtained values from Cs_3Sb cathodes at room temperatures Cultrera *et al.* (2011). Fig. 3.7 shows the comparison of MTE at incident photon energies very close to and below the threshold at both room temperature and cryogenic temperature of 90 K [Cultrera *et al.* (2015)]. It can be seen that the calculated values of MTE from our model are in close agreement with those observed experimentally
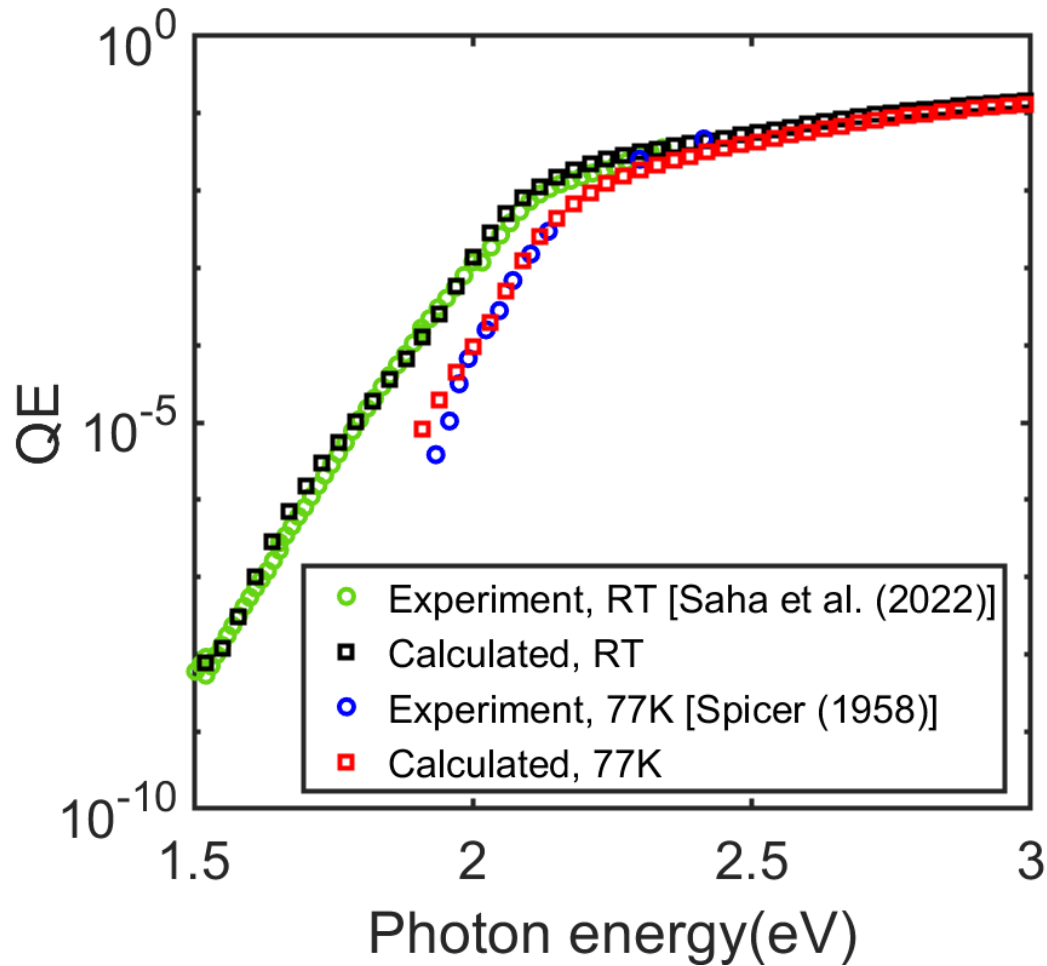
Figure 3.5: QE of Cs3Sb Cathode as a Function of Photon Energy, Calculated at 300 K and 77 K Using Our Model (Equation 3.15). Experimental Measurements of QE at 300 K [Saha *et al.* (2022)] and 77 K [Spicer (1958)] Are Shown For Comparison. The Exponentially Decaying Tail in QE below the Threshold Is Due to the Exponentially Decreasing Defect Density of States with Increasing Energy. In the Absence of Defect States, the QE Should Drop to Zero Right at the Threshold. The Experimental QE Data at RT Have Been Reproduced with Permission from Saha Et Al., Appl. Phys. Lett. 120, 194102 (2022). Copyright 2022 Aip Publishing LLC.

at low/negative excess energies.

Thus, we see that our theoretical model predicts that cathodes with disordered surfaces and defect states in the bulk, when operated near the threshold may yield MTE values, which are above $k_B T$ even below the threshold. Furthermore, these higher MTE values are related to the exponential decay of the defect density of states, which also determines the exponential decay of the QE below the threshold. Thus, cathodes with a longer QE decay below the threshold can be expected to have a higher MTE at or below the threshold. This increase in MTE will be beyond the increase caused due to the surface roughness of such cathodes.

3.5   Conclusion

We have developed a new photoemission model based on Spicer's three step formalism to explain photoemission from photocathodes with disordered surfaces. Our model obtains the same QE and MTE relationships as the D-S scheme without the need to use unphysical assumptions like parabolic dispersion relations or conservation of transverse momentum and can be applied to metals as well as semiconductor cathodes.

We have used this model to obtain a theoretical understanding of photoemission from polycrystalline alkali-antimonide photocathodes at photon energies close to and below the threshold. Below the threshold, photoemission is due to excitation of electrons from states populated with electrons from the Fermi tail as well as an exponentially decaying density of states above the VBM caused due to defects and impurities. Our model predicts values of QE and MTE from such polycrystalline Cs_3Sb cathodes, which are in excellent agreement with those observed experimentally at both room and cryogenic temperatures. This also suggests that the MTE from such cathodes may not reach the thermal limit, when operated near the threshold due to such defect states and a more detailed study of the effects of such defect states on MTE is necessary to maximize brightness of electron beams.
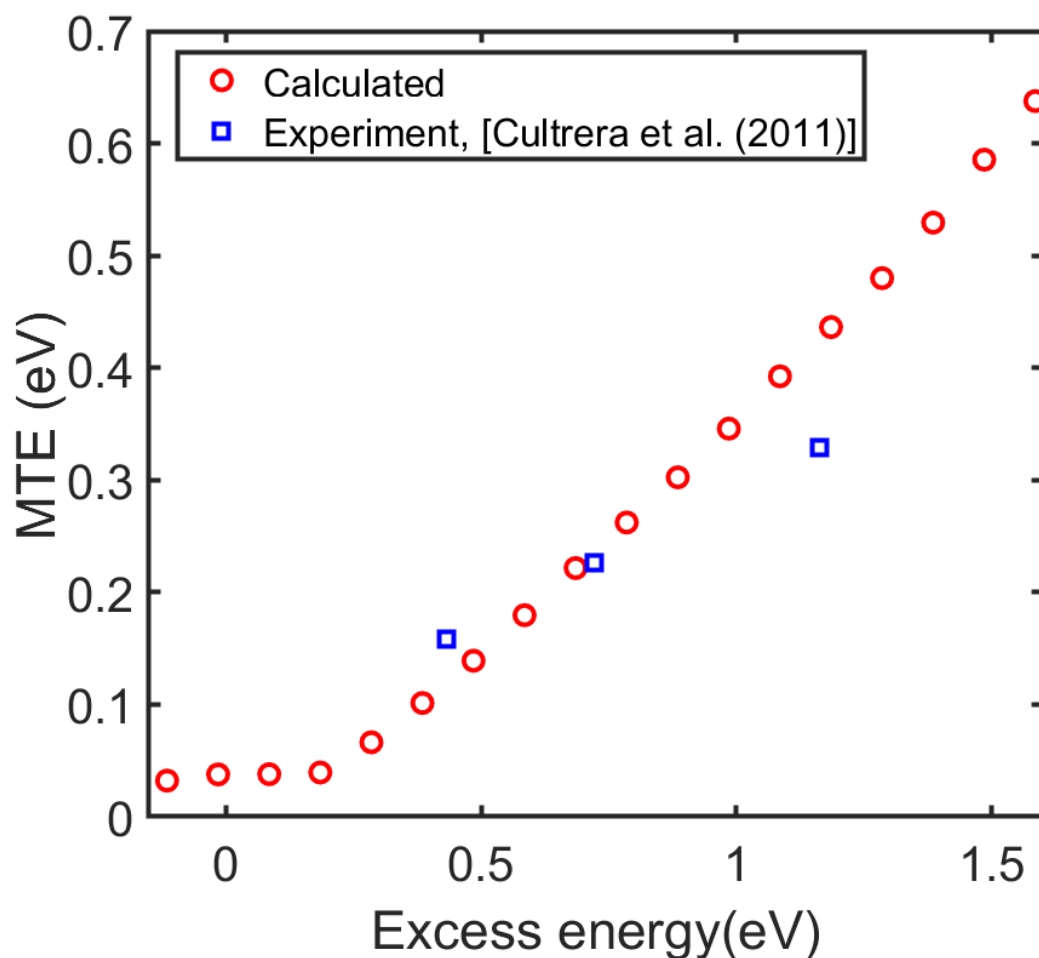
Figure 3.6: MTE of Cs_3Sb Cathode as a Function of Excess Energy, Calculated at Higher Excess Energies Using Our Model (Equation 3.17). Experimental MTE data [Cultrera *et al.* (2011)] at Higher Excess Energies are Shown for Comparison. The Deviations Between the Calculated and Experimental Results can be Attributed to Electron-Phonon Scattering Suring Transport. The Experimental MTE Data Have Been Reproduced with Permission from Cultrera et al., App. Phys. Lett. 99, 152110(2011). Copyright 2011 AIP Publishing LLC.
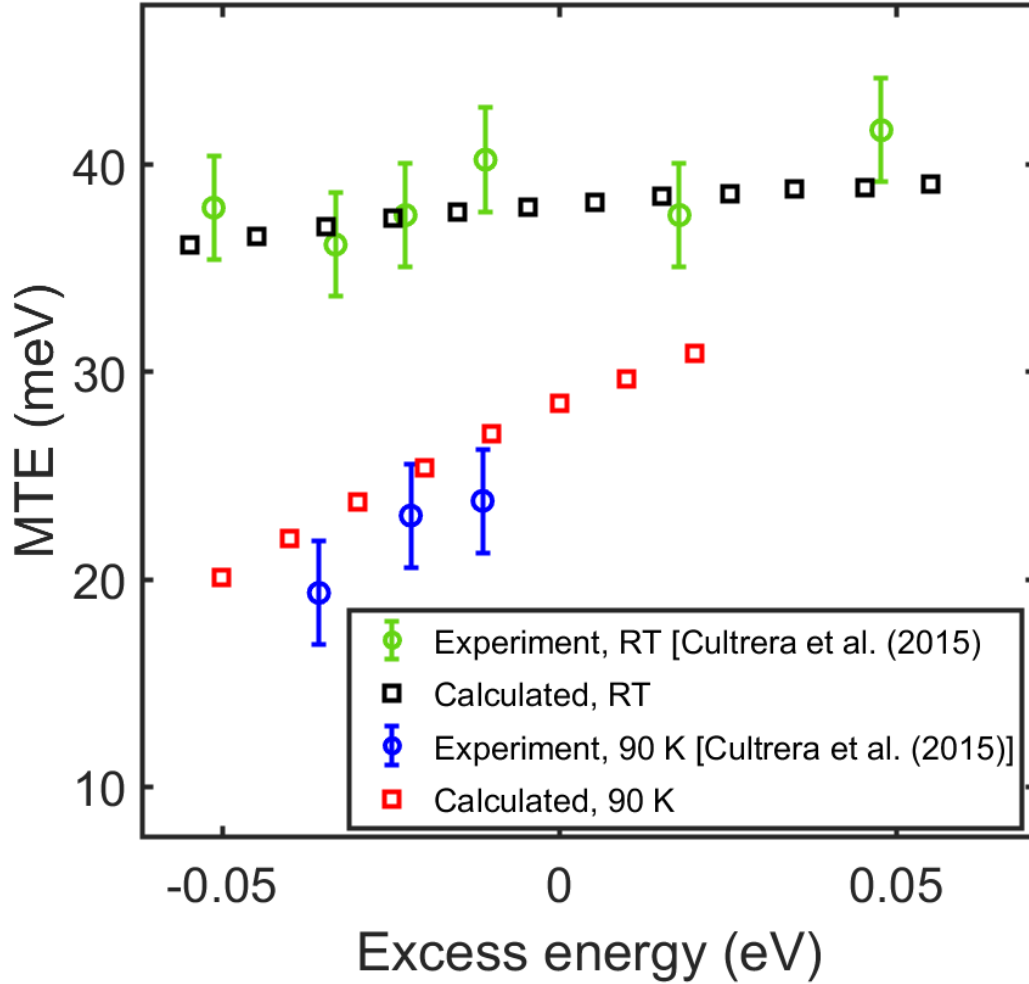
Figure 3.7: MTE of Cs₃Sb Cathode as a Function of Excess Energy, Calculated Near Threshold at 300 K and 90 K Using Our Model (Equation 3.17). Experimental Measurements of MTE at 300 K [Ref. 25] and 90 K [Ref. 25] Are Shown for Comparison. Our Model Predicts Near Threshold MTE Values Which Are Higher than the Thermal Limit of k_BT, Due to Emission From Defect Density of States. The Experimental Data Have Been Reproduced with Permission from Cultrera et al., Phys. Rev. Spec. Top. Accel. Beams. 18, 113401 (2015). Copyright 2015 Author(s), Licensed under a Creative Commons Attribution (CC BY) license.

3.6 Acknowledgements

3.7 References

Bae, J., I. Bazarov, L. Cultrera, J. Maxson, P. Musumeci, X. Shen, S. Karkare and H. Padmore, "Multi-photon photoemission and ultrafast electron heating in cu photocathodes at threshold", TUPML026 (2018).

Bergund, C. N. and W. E. Spicer, "Photoemission studies of copper and silver: Theory", Phys. Rev. **136**, A1030 (1964).

Chubenko, O., S. Karkare, D. A. Dimitrov, J. K. Bae, L. Cultrera, I. Bazarov and A. Afanasev, "Monte carlo modeling of spin-polarized photoemission from p-doped bulk gaas", J. Appl. Phys. **130**, 063101 (2021).

Cultrera, L., I. Bazarov, A. Bartnik, B. Dunham, S. Karkare, R. Merluzzi and M. Nichols, "Thermal emittance and response time of a cesium antimonide photocathode", Applied Physics Letters **99**, 15, 152110 (2011).

Cultrera, L., C. Gulliford, A. Bartnik, H. Lee, and I. Bazarov, "Ultra low emittance electron beams from multi-alkali antimonide photocathode operated with infrared light", Appl. Phys. Lett. **108**, 134105 (2016).

Cultrera, L., S. Karkare, H. Lee, X. Liu, I. Bazarov and B. Dunham, "Cold electron beams from cryocooled, alkali antimonide photocathodes", Physical Review Special Topics-Accelerators and Beams **18**, 11, 113401 (2015).

Dowell, D. H., F. K. King, R. E. Kirby, J. F. Schmerge and J. M. Smedley, "In situ cleaning of metal cathodes using a hydrogen ion beam", Physical Review Special Topics-Accelerators and Beams **9**, 6, 063502 (2006).

Dowell, D. H. and J. F. Schmerge, "Quantum efficiency and thermal emittance of metal photocathodes", Phys. Rev. ST Accel. Beams. **12**, 074201 (2009).

Feng, J., S. Karkare, J. Nasiatka, S. Schubert, J. Smedley and H. Padmore, "Near atomically smooth alkali antimonide photocathode thin films", Journal of Applied Physics **121**, 4, 044904 (2017).

Feng, J., J. Nasiatka, W. Wan, S. Karkare, J. Smedley and H. A. Padmore, "Thermal limit to the intrinsic emittance from metal photocathodes", Applied Physics Letters **107**, 13, 134101 (2015).

Gevorkyan, G. S., S. Karkare, S. Emamian, I. V. Bazarov and H. A. Padmore, "Effects of physical and chemical surface roughness on the brightness of electron beams from photocathodes", Phys. Rev. Accel. Beams. **21**, 093401 (2018).

Gruner, S. M., D. Bilderback, I. Bazarov, K. Finkelstein, G. Krafft, L. Merminga, H. Padamsee, Q. Shen, C. Sinclair and M. Tigner, "Energy recovery linacs as synchrotron radiation sources", Review of Scientific Instruments **73**, 3, 1402–1406 (2002).

Gupta, P., L. Cultrera and I. Bazarov, "Monte carlo simulations of electron photoemission from cesium antimonide", J. Appl. Phys. **121**, 215702 (2017).

Hüfner, S., "Photoelectron spectroscopy, principles and applications", URL https://link.springer.com/book/10.1007/978-3-662-09280-4/ (2003).

Jensen, K. L., J. J. Petillo, E. J. Montgomery, Z. Pan, D. W. Feldman, P. G. O'Shea, N. A. Moody, M. Cahay, J. E. Yater and J. L. Shaw, "Application of a general electron emission equation to surface nonuniformity and current density variation", Journal of Vacuum Science & Technology B: Microelectronics and Nanometer Structures Processing, Measurement, and Phenomena **26**, 2, 831–837 (2008).

Karkare, S., G. Adhikari, W. A. Schroeder, J. K. Nangoi, T. Arias, J. Maxson and H. Padmore, "Ultracold electrons via near-threshold photoemission from single-crystal cu (100)", Physical review letters **125**, 5, 054801 (2020).

Karkare, S. and I. Bazarov, "Effects of surface nonuniformities on the mean transverse energy from photocathodes", Physical Review Applied **4**, 2, 024015 (2015).

Karkare, S., D. Dimitrov, W. Schaff, L. Cultrera, A. Bartnik, X. Liu, E. Sawyer, T. Esposito and I. Bazarov, "Monte carlo charge transport and photoemission from negative electron affinity gaas photocathodes", Journal of Applied Physics **113**, 10, 104904 (2013).

Kiziroglou, M., X. Li, A. Zhukov, P. De Groot and C. De Groot, "Thermionic field emission at electrodeposited ni–si schottky barriers", Solid-State Electronics **52**, 7, 1032–1038 (2008).

Maxson, J., P. Musumeci, L. Cultrera, S. Karkare and H. Padmore, "Ultrafast laser pulse heating of metallic photocathodes and its contribution to intrinsic emittance", Nuclear Instruments and Methods in Physics Research Section A: Accelerators, Spectrometers, Detectors and Associated Equipment **865**, 99–104 (2017).

Musumeci, P., J. G. Navarro, J. Rosenzweig, L. Cultrera, I. Bazarov, J. Maxson, S. Karkare and H. Padmore, "Advances in bright electron sources", Nuclear Instruments and Methods in Physics Research Section A: Accelerators, Spectrometers, Detectors and Associated Equipment **907**, 209–220 (2018).

Nangoi, J., M. Gaowei, A. Galdi, J. Maxson, S. Karkare, J. Smedley and T. Arias, "Ab initio study of the crystal and electronic structure of mono-and bi-alkali antimonides: Stability, goldschmidt-like tolerance factors, and optical properties", arXiv preprint arXiv:2205.14322 (2022).

Nguyena, T. H. and S. K. O'Leary, "The dependence of the fermi level on temperature, doping concentration, and disorder in disordered semiconductors", J. Appl. Phys. **88**, 3479 (2000).

Oudheusden, T. V., E. F. de Jong, S. B. van der Geer, W. O. 't Root, O. J. Luiten and B. J. Siwick, "Electron source concept for single-shot sub-100 fs electron diffraction in the 100 kev range", J. Appl. Phys. **102**, 093501 (2007).

Pierce, C. M., J. K. Bae, A. Galdi, L. Cultrera, I. Bazarov and J. Maxson, "Beam brightness from cs–te near the photoemission threshold", Appl. Phys. Lett. **118**, 124101 (2021).

Rosenzweig, J., N. Majernik, R. Robles, G. Andonian, O. Camacho, A. Fukasawa, A. Kogar, G. Lawler, J. Miao, P. Musumeci *et al.*, "An ultra-compact x-ray free-electron laser", New Journal of Physics **22**, 9, 093067 (2020).

Sa-yakanit, V. and H. Glyde, "Urbach tails and disorder", Comments Condens. Matter Phys. **1(13)**, 35–48 (1987).

Saha, P., O. Chubenko, G. S. Gevorkyan, A. Kachwala, C. J. Knill, C. Sarabia-Cardenas, E. Montgomery, S. Poddar, J. T. Paul, R. G. Hennig *et al.*, "Physically and chemically smooth cesium-antimonide photocathodes on single crystal strontium titanate substrates", Applied Physics Letters **120**, 19, 194102 (2022).

Saha, P., O. Chubenko, J. K. Nangoi, T. Arias, E. Montgomery, S. Poddar, H. A. Padmore and S. Karkare, "Theory of photoemission from cathodes with disordered surfaces", Journal of Applied Physics **133**, 6 (2023).

Spicer, W. and A. HerreraGómez, "Modern theory and applications of photocathodes", Proc. SPIE 2022, Photodetectors and Power Meters, (1993).

Spicer, W. E., "Photoemissive, photoconductive, and optical absorption studies of alkali-antimony compounds", Physical review **112**, 1, 114 (1958).

Vecchione, T., D. Dowell, W. Wan, J. Feng and H. Padmore, "Quantum efficiency and transverse momentum from metals", Proceedings of FEL 2013, New York, NY (2013).

Chapter 4

THERMAL LIMIT TO THE MEAN TRANSVERSE ENERGIES FROM CESIUM-ANTIMONIDE PHOTOCATHODES

4.1 Abstract

Quantum efficiency (QE) and mean transverse energy (MTE) of the electrons emitted from the photocathodes determine the quality of electron bunches required for various photoinjector applications. Alkali-antimonides are an interesting class of semiconductor photocathodes, which have emerged as potential candidates for electron sources required for various photoinjector applications. In this work, we present a detailed measurement of photoemission electron energy spectra (PEES), MTE and QE near the photoemission threshold from Cs_3Sb, one of the most promising alkali-antimonide photocathode materials. Our PEES measurements indicate a low photoemission threshold of around 1.5 eV, which is in contrast with the previously perceived threshold of 1.8-2.0 eV. At the measured threshold, the MTE nearly converges to the thermal limit of k_BT at 300 K. Moreover, at 1.8 eV, the MTE was measured to be $\sim$40 meV which is comparable to the previously reported value. This higher than k_BT value of MTE is not due to surface roughness effects as previously thought, but it is simply a consequence of excess energy at 1.8 eV.

4.2 Introduction

A wide range of linear-accelerator applications like x-ray free electron lasers (XFEL) [Emma *et al.* (2010)], ultrafast electron diffraction (UED) [Sciaini and Miller (2011)] and energy recovery linacs (ERL) [Gruner *et al.* (2002)] require dense and coherent electron beams for their operation. High density bunched electron beams required for the operation

51

of the above mentioned instruments are typically produced using photoinjectors. Photoinjectors essentially consist of a thin photoemissive material (photocathode) placed in a large accelerating field gradient, which is typically in the range of 1-100 MV/m, depending on the design of the photoinjector [Power (2010); Russell (2003)].

The performance of the photocathode used for photoinjector applications is dependent on the quality of the electron bunch generated from it. A figure of merit that determines the quality of electron bunch is given by the the brightness of the electron bunch. The maximum achievable brightness of the electron bunch in a photoinjector scales according to the following relation [Bazarov *et al.* (2009)]:

$$B \propto \frac{\mathscr{E}^n}{\text{MTE}}, \tag{4.1}$$

where n is the real number between 1 and 2, $\mathscr{E}$ is the applied electric field at the cathode and MTE is the mean transverse energy of the emitted electrons. The maximum possible electric field is set by the design of the photoinjector. As a result, to further increase the brightness of the emitted electron bunch, we need to reduce the MTE of the emitted electrons [Musumeci *et al.* (2018)].

The MTE is a property of the cathode material, its surface, the drive laser wavelength and laser fluence [Dowell and Schmerge (2009)]. The MTE from the cathodes is typically proportional to one-third of the excess energy [Dowell and Schmerge (2009); Saha *et al.* (2023)], where excess energy is defined as the difference in energy between the incident photon energy and the work function of the material. For photon energies close to the threshold i.e. low or negative excess energies, the MTE gets limited by the Fermi tail of the electron distribution to $k_B T$ [Vecchione *et al.* (2013)], where k_B is the Boltzmann constant and T is the lattice temperature of the cathode. The thermal limit of $k_B T$ has been experimentally demonstrated for polycrystalline Sb thin films at room temperature [Feng *et al.* (2015)]. There has also been experimental demonstration of a record low MTE of 5

52

meV from cryo-cooled surface of Cu(100) [Karkare *et al.* (2020)] and a low MTE of 10 meV at 77 K from graphene-coated Cu(110) [Knill *et al.* (2023)]. However, metal cathodes due to their very low quantum efficiency (QE) in the range of 10^{-6}-10^{-8} at threshold energies, are inefficient electron sources for many photoinjector applications [Dowell *et al.* (2010); Musumeci *et al.* (2018)]. Given the low QE, higher laser fluences need to be used to extract the required charge densities, resulting in non-linear photoemission processes [Maxson *et al.* (2017); Bae *et al.* (2018)]. Such non-linear processes increase the MTE to few 100's of meV, thereby significantly reducing the brightness of the emitted electron bunch.

One way of circumventing the MTE degrading effect of non-linear photoemission is by the use of high QE, low electron-affinity semiconductor cathodes like alkali and bi-alkali antimonides such as Cs_3Sb, K_2CsSb, Na_2KSb etc. Due to their relatively high QE exceeding 1% in the visible wavelengths, this class of semiconductor photocathodes has emerged as potential candidates for the next generation light sources and accelerator applications. The intrinsic property of high QE of alkali-antimonides has been leveraged to generate the highest average current [Dunham *et al.* (2013)]. A low MTE has been achieved from alkali-antimonide photocathodes by illuminating them with near-threshold photons, at room and cryogenic temperatures [Cultrera *et al.* (2015)]. However, alkali-antimonide are typically grown as polycrystalline thin films with nanoscale surface roughness. The roughness and the resulting work function variations along with defects can limit the smallest achievable MTE from alkali-antimonides [Gevorkyan *et al.* (2018); Saha *et al.* (2023)]

Of all the high QE alkali-antimonides, Cs_3Sb has the least number of constituent elements, which makes its growth process the easiest. Therefore, Cs_3Sb cathodes have been studied extensively to investigate their photoemission properties and achieve smooth, well-ordered surfaces. Using the co-deposition technique on single crystalline strontium titanate substrates, atomically flat and uniform surfaces of Cs_3Sb have been achieved [Saha *et al.*

(2022)]. Recently, the growth of a single crystal film of Cs_3Sb on 3C-SiC has been demonstrated [Parzyck *et al.* (2022)]. It was expected that such surfaces would result in MTE limited by k_BT at the threshold along with a high QE ($> 10^{-4}$).

Based on the knee observed in the log plot of the QE spectral response, previous works have deduced the photoemission threshold of the Cs_3Sb cathodes to be 1.8-2.0 eV [Cultrera *et al.* (2011, 2015); Saha *et al.* (2022)]. At this perceived threshold, the MTE from the Cs_3Sb cathodes was measured to be 40 meV at 300 K and 22 meV at 90 K, significantly larger than the thermal limit at both of the temperatures. This larger MTE has been attributed to the surface roughness effects [Feng *et al.* (2017); Smedley *et al.* (2015); Karkare and Bazarov (2015); Gevorkyan *et al.* (2018)] and bulk defect density of states [Spicer (1958); Saha *et al.* (2023)].

In this paper, we present detailed MTE, photoemission electron energy spectra (PEES) and QE measurements in the spectral range of 1.45-2.33 eV photon energy. Our PEES measurements conclusively show that the work function of Cs_3Sb cathodes is around 1.5 eV. Further, we show that at the threshold of 1.5 eV, the MTE does reach the k_BT value at room temperatures. Moreover, our measurements show that the higher than k_BT value of MTE measured and reported in previous works at 1.8 eV is not due to roughness/ surface non-uniformity effects and defect density of states, but is simply an effect of the excess energy at 1.8 eV. Our measurements also show that the MTE doesn't follow the (excess energy)/3 trend as was previously thought to be the case based on a threshold of 1.8-2.0 eV. The values of MTE measured are significantly lower owing to the energy losses due to strong scattering effects during the transport of the excited electrons to the surface before emission [Karkare *et al.* (2013)].

4.3 Experiment

The Cs_3Sb cathodes studied in this paper were grown on 2 substrates: doped silicon (Si) and Nb-doped strontium titanate (STO). Prior to the growth, the substrates were rinsed with isopropyl alcohol and annealed at 450 °C for 2-3 hours in an ultra-high-vacuum (UHV) chamber with a base pressure in the low 10^{-10} torr range. The Cs_3Sb cathodes were grown via co-deposition of Cs and Sb on the Si and STO substrates. By shining a 5 mW green laser, the photocurrent emitted from the cathode was measured during the growth to calculate the QE, which serves as a feedback to monitor the growth and performance of the cathodes. Figure 4.1 represents the evolution of QE during the growth of Cs_3Sb cathodes on Si and STO substrates. The growth was terminated by turning down the source heaters once the QE began to plateau/drop. The final QE of the Cs_3Sb cathodes was between 3-4 % in green (λ = 530 nm). The two cathodes grown on Si and STO substrates were estimated to have a thickness of $\sim$ 40 nm. Further details of the growth process can be found in [Saha *et al.* (2022)]. Based on previous AFM measurements, the film on Si is expected to have an rms roughness of $\sim$ 1.4 nm, whereas the growth on STO is expected to be significantly different and smoother with an rms roughness of $\sim$ 0.3-0.6 nm [Saha *et al.* (2022)].

After growth, the two Cs_3Sb cathodes on Si and STO substrates were transported via a UHV transfer line into the PEEM, using which the QE, PEES and MTE measurements of the Cs_3Sb cathodes were performed [Foc (2023)]. The pressure in the transfer line was in 10^{-10} torr range and no QE degradation was observed during the transfer. The base pressure of the PEEM chamber was also in the low 10^{-10} torr range during the measurements. A detailed description of the measurement procedure can be found in Ref. Kachwala *et al.* (2022). All the measurements were performed using a 500 kHz repetition rate femtosecond pulsed laser with a pulse length of 150 fs generated from Optical Parametric Amplifier (Light Conversion Orpheus pumped by Light Conversion Pharos). The fluence of the laser
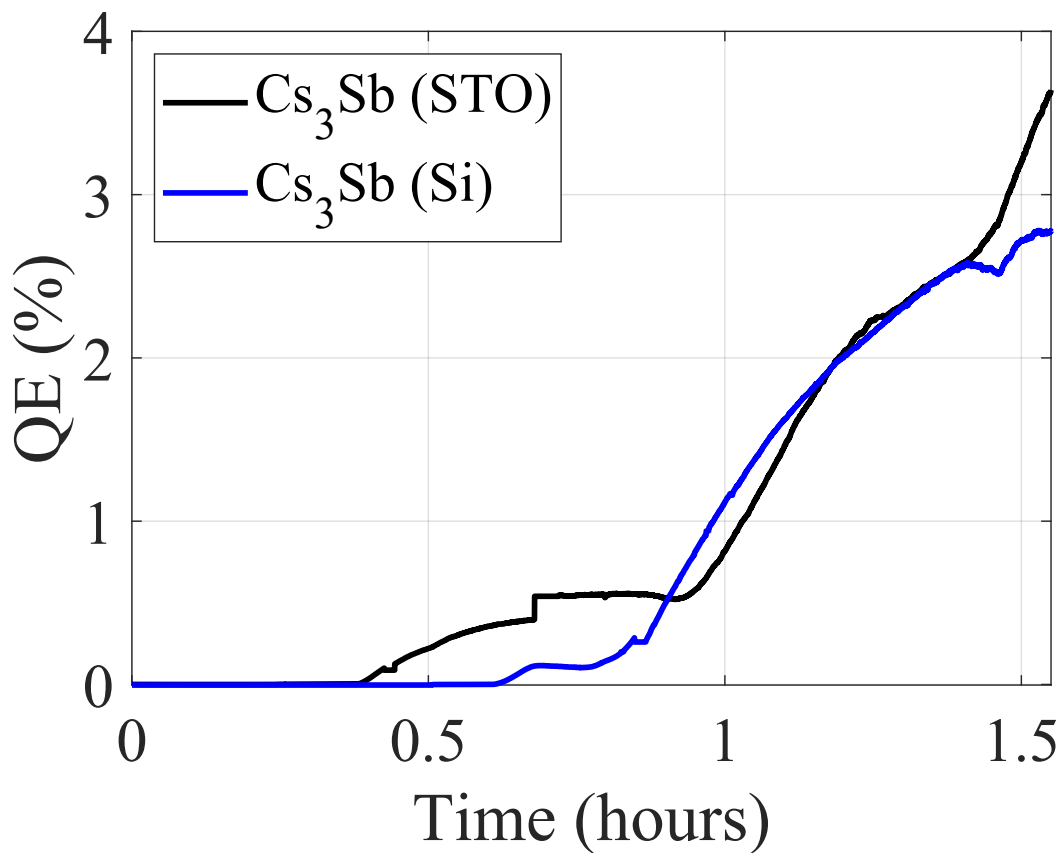
Figure 4.1: Evolution of QE During Growth of Cs₃Sb Cathodes on Si and Doped STO Substrates.

pulses incident on the sample was kept small enough to ensure linear electron counts and avoid effects of space charge and non-linear photoemission.

4.4 Results and Discussions

Figure 4.2 shows an experimentally determined PEES for the Cs₃Sb cathodes on (a) Si and (b) Nb-doped STO substrates. For both the cathodes, the PEES broaden in kinetic energy with the increasing photon energy. Taking the maximum kinetic energy to be 1% of the maxima of the energy distribution curve, the x-intercept from the plot of maximum kinetic energy vs photon energy gives us the work function (Φ) of the photocathode. This is shown in the inset of Figure 4.2. The value of Φ obtained from the PEES data is 1.5 eV,
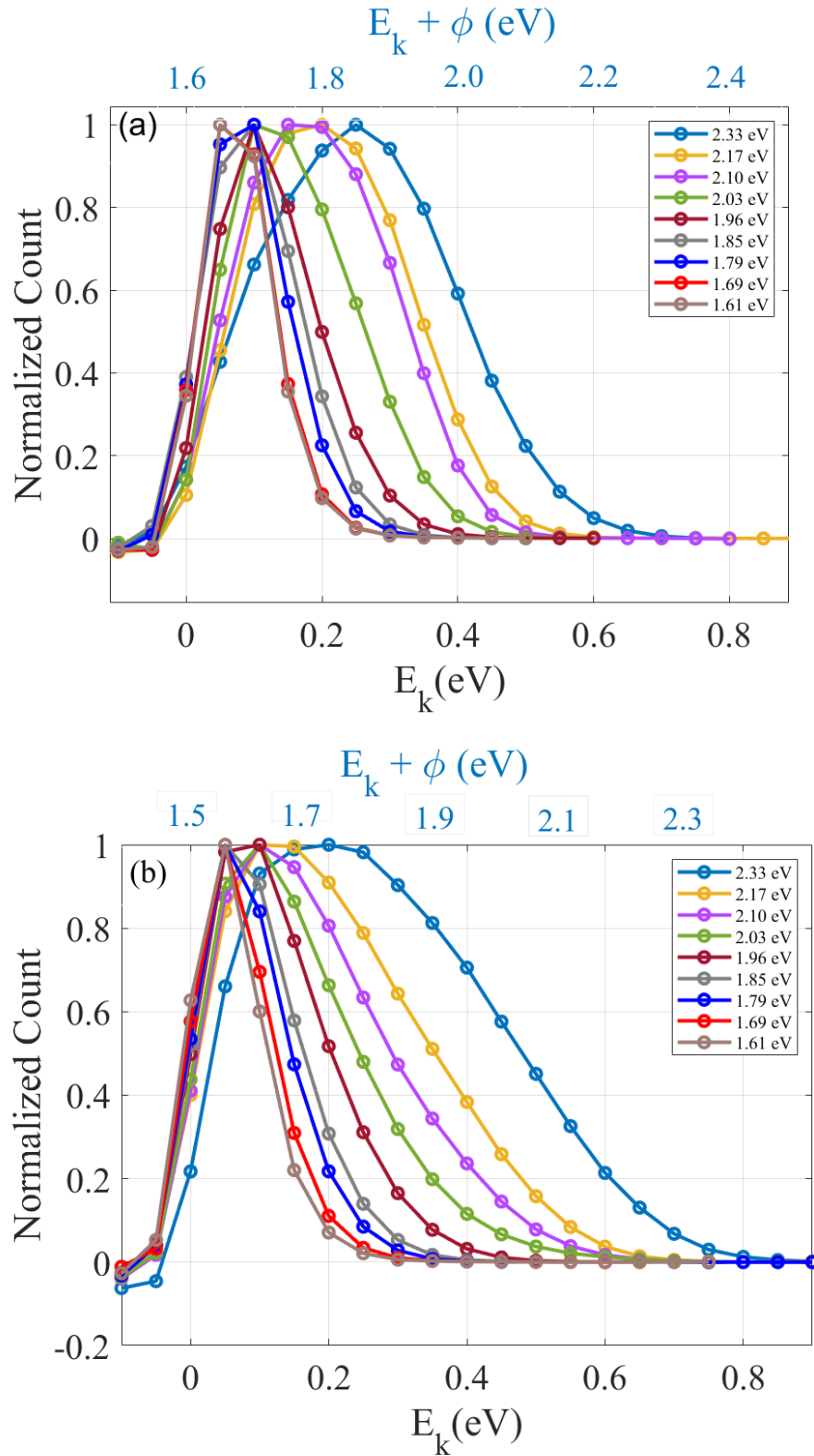
chch

Figure 4.2: Photoemission Electron Energy Spectra (PEES) at Different Incident Photon Energies for the Cs_3Sb Film Grown on: (a) Si and (b) Doped STO substrates. The Bottom x-axis Represents the Kinetic Energy of the Emitted Electrons and the Top x-axis Represents the Sum of the Kinetic Energy of the Emitted Electrons and the Work Function (Φ) of the Photocathode Sample.

with an uncertainty of ~ 0.1 eV in the measurement. This is in contrast to the work function of 1.8-2.0 eV that is typically assumed based on the QE spectral response [Cultrera *et al.* (2015); Saha *et al.* (2022)]. Such a low value of the work function has also been reported based on energy distribution measurements in the literature by Sakata (1953).
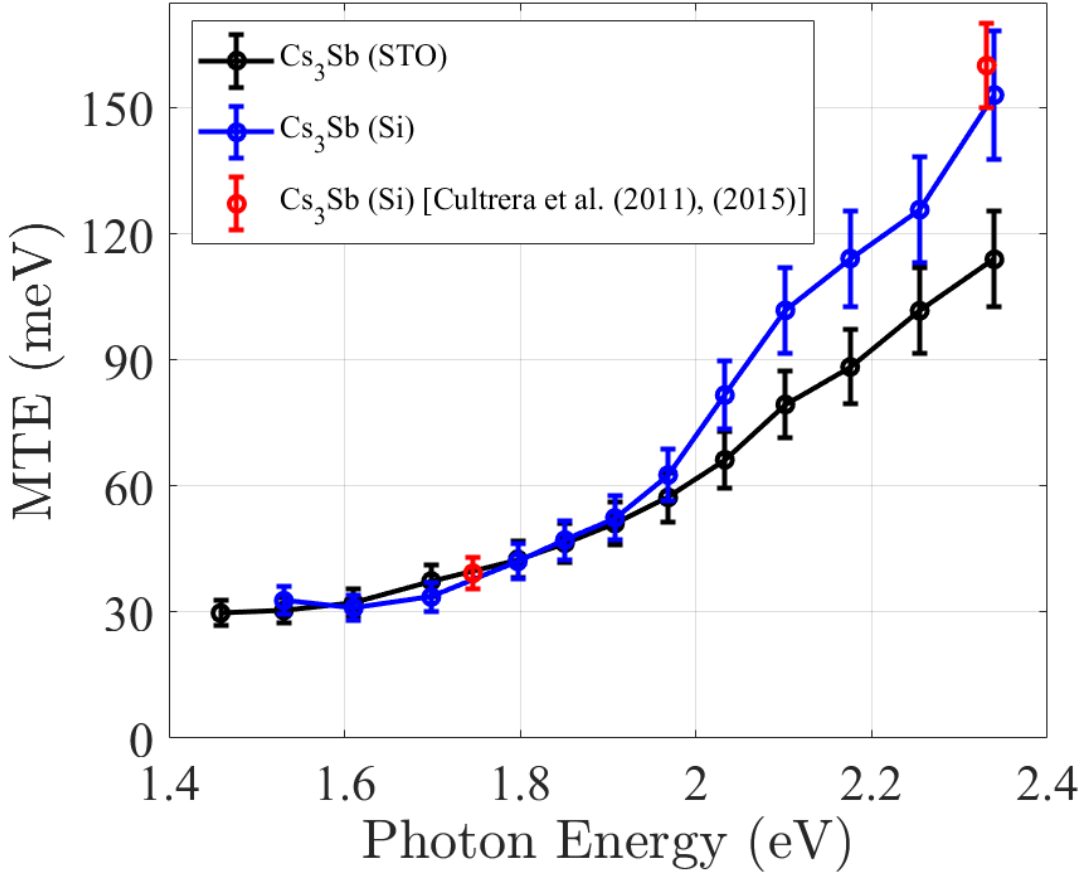
Figure 4.3: Spectral Response of MTE On Si and Doped STO substrates. The MTE Approaches $k_B T$ at the Threshold. At Higher Photon Energies, MTE Does Not Scale As One-third of the Excess Energy Owing to the Scattering Losses, Which the Electrons Suffer Before Emission. The Red Dots Show Measurements of MTE From Cs_3Sb (Si) Reported by Previous Authors. Our Results are in Perfect Agreement with Previous Results. The Experimental MTE Data Marked by Red Dots Have Been Reproduced with Permission from Cultrera Et Al., App. Phys. Lett. 99, 152110 (2011) [Copyright 2011 AIP Publishing LLC.] and Cultrera Et Al., Phys. Rev. Spec. Top. Accel. Beams. 18, 113401 (2015) [Copyright 2015 Author(s), Licensed under a Creative Commons Attribution (CC BY) License].

The low work function $\Phi \sim (1.5 \pm 0.1)$ eV has been further corroborated by the MTE

data measured from the Cs_3Sb cathodes. Figure 4.3 shows the spectral response of MTE measured at room temperature from the Cs_3Sb cathodes grown on Si and STO substrates under electric fields ~ 0.5 MV/m. The MTE was measured to be ~ 30 meV at photon energies equal to the work function of the Cs_3Sb cathodes. Within the limit of instrumental error, the experimentally measured value of MTE thus, nearly converges to the thermal limit of $k_B T$, which is 25 meV at room temperature. At a photon energy of 1.75 eV, which was earlier reported to be the photoemission threshold, the MTE is measured to be ~ 40 meV which is consistent with previously reported data [Cultrera *et al.* (2015)]. Based on the results that we have obtained, we claim that the higher than $k_B T$ values of MTE are not due to surface non-uniformities and defect density of states, it is a consequence of excess energy.

At photon energies away from the photoemission threshold, it can be seen in Figure 4.3 that the MTE does not scale as one-third of the excess energies. This can be explained by the scattering losses which the electrons suffer with different charge carriers and defects during transport to the surface before getting emitted. Also, at higher photon energies the Cs_3Sb cathode grown on STO substrate exhibits a lower value for MTE than the corresponding cathode grown on Si substrate. Previous studies have shown that the growth on the two substrates leads to very different surfaces [Saha *et al.* (2022)]. It is possible that the two films have a very different grain/defect structure, which can potentially result in higher scattering and therefore, larger electron energy losses in the film grown on the STO substrates as compared to films grown on Si.

Furthermore, the scattering as evidenced by the deviation of MTE values from (excess energy)/3 curve, is reflected in the PEES data. The top x-axis in Figure 4.2 shows the sum of kinetic energy (E_k) of the emitted electrons and the work function (Φ) of the photocathodes. The sum of the maximum kinetic energy of the emitted electrons and the work function approximately equals to the photon energy. If electrons do not scatter before emission or

59

if the scattered electrons lose enough energy to not get emitted, like the case of metallic photocathodes, the maximum in the energy distribution curves corresponds to the fermi edge drop. This fermi edge drop occurs at nearly the photon energy on the kinetic energy (E_k) + work function (Φ) axis [Sun *et al.* (2011)]. In Figure 4.2, we can see that the sum of the work function and the kinetic energy corresponding to the maximum of the energy distribution curves does not coincide with that of the photon energy. This indicates that the electrons are scattered during transport, before being emitted from the Cs_3Sb cathodes. A similar electron scattering mechanism is observed for other semiconductor photocathodes [Sun *et al.* (2011); Kachwala *et al.* (2022)].
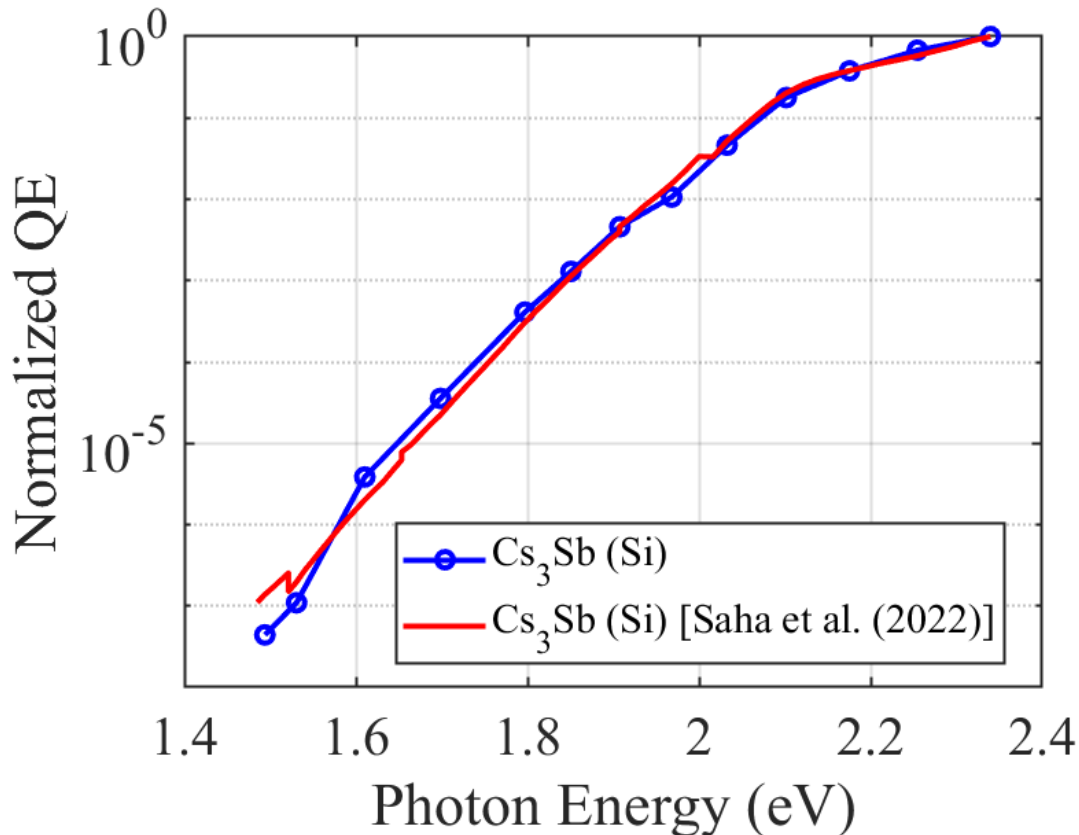
Figure 4.4: Comparison of Spectral Response of QE from Cs_3Sb Cathodes on Si, Measured using PEEM and Compared to Cathode Reported in Ref. 15. The QE is Normalized to the Maximum QE Obtained from the Cs_3Sb Cathode in Green. The Experimental QE Data Corresponding to the Red Curve has been Reproduced from Saha Et Al., Appl. Phys. Lett. 120, 194102 (2022). Copyright 2022 AIP Publishing LLC.

Lastly, the spectral response of QE was measured with PEEM from the Cs_3Sb cathode on Si substrate and compared with previously reported data in Figure 4.4. A knee like feature is observed ~ 2.0 eV, which has been earlier observed and reported in QE profiles from the Cs_3Sb cathodes. At the actual threshold of 1.5 eV, the QE measured is very low in the order of 10^{-7}, making it impractical to operate Cs_3Sb cathodes at the threshold for large charge density applications, without encountering non-linear photoemisison effects.

Previously this knee was thought to be the work function. The knee can imply the presence of direct band gap or band-bending at the surface. This calls for further investigation into the band structure and optical properties of Cs_3Sb cathodes. Use of detailed Monte Carlo simulations will be essential to model the scattering effects and fully explain the measured photoemission properties. The photoemisison and optical properties of single crystalline Cs_3Sb [Parzyck et al. (2022)] could also be very different from the polycrystalline films measured here and warrant exploration.

Cs_3Sb is composed of only two elements. This makes its growth process significantly easier compared to other alkali-antimonides. However, it is much more complex in terms of lattice and electronic structure compared to other high QE alkali-antimonides. A recent study based on using ab-initio calculations has shown that Cs_3Sb is thermodynamically unstable in its $D0_3$ cubic structure [Nangoi et al. (2022)], and it requires a distorted superlattice to exist in the stable form. This stable form of Cs_3Sb has a significantly different electronic structure compared to the $D0_3$ cubic Cs_3Sb. The electronic structure of Cs_3Sb is still not well understood, and there can be exotic physics at play which has resulted in the observed QE, MTE and PEES data. Other high QE alkali-antimonides like K_2CsSb and Na_2KSb, although more complex to grow in a smooth fashion, are expected to be stable in the $D0_3$ form [Nangoi et al. (2022)]. The electronic structures of those alkali-antimonides may be more predictable and their near-threshold photoemisison properties could be significantly different and warrant exploration.

4.5 Conclusion

In conclusion, we measured PEES, MTE and QE of Cs_3Sb photocathodes in the photon energy range of 1.45-2.33 eV. The PEES indicate that the work function of the Cs_3Sb cathodes is $\sim$ 1.5 eV. From the PEES we observed that the sum of work function and kinetic energy corresponding to the maxima in the emission spectrum does not match the excitation energy. This indicates that the scattering of electrons influences the emission. The MTE does not scale as one-third of the excess energy. This observed trend in MTE is due to the scattering of electrons with phonons, defects and other charge carriers during transport to the surface before getting emitted. The MTE decreases with the decrease in excess energy and shows a flat trend near the threshold, which was observed to be $\sim$30 meV comparable to thermal energy at 300 K. Despite the low MTE, it might not be feasible to operate these cathodes at the threshold given their low QE of the order of 10^{-7} (comparable to metal cathodes). As a result, the cathodes may need to be operated at photon energies away from the threshold, which would lead to higher MTE as a consequence of higher excess energy. Epitaxial, single-crystalline Cs_3Sb cathodes and other alkali-antimonides may, however, exhibit different photoemission features when operated at the threshold. It would be worthwhile to pursue photoemission studies of these cathodes to pave the way for brighter electron beams.

4.6 Acknowledgements

Chapter 5

ION-BEAM ASSISTED GROWTH OF ALKALI-ANTIMONIDE PHOTOCATHODES

5.1 Abstract

We report on the novel use of a Cs^+ ion gun for an ion-beam-assisted molecular-beam-epitaxy (IBA-MBE) method to sequentially deposit Cs_3Sb cathodes on room temperature substrates as opposed to the standard technique of thermal evaporation on elevated-temperature substrates. The details of the ultra-high-vacuum chamber, the Cs^+ ion source and the growth technique are elaborated. The final QE is high for Cs_3Sb cathodes grown on two different substrates – Si (100) and strontium titanate – and is comparable to the QE of cathodes grown using thermal sources. This suggests IBA-MBE could be a viable alternative to grow alkali-antimonides without substrate heating, paving the way for the growth of epitaxial alkali-antimonides in a more reproducible fashion, which may help improve the efficiency of photon detectors and accelerator applications that use alkali-antimonides as electron sources.

5.2 Introduction

The family of alkali-antimonide materials, which includes Cs_3Sb, K_2CsSb, Na_2KSb etc, has been extensively used for decades in photon detection applications and imaging devices such as photomultiplier tubes and night vision cameras due to their inherent high quantum efficiency (QE) in the visible range of the spectrum [Musumeci *et al.* (2018)]. During the last two decades, alkali-antimonides have risen to prominence as efficient sources of electrons to drive 4th generation x-ray sources such as energy recovery linacs (ERL) [Gruner *et al.* (2002)] and x-ray free electron lasers (XFEL) [Emma *et al.*

63

(2010)], nuclear and high energy physics experiments (for example, electron ion collider [Michizono (2019)] and electron cooling of hadron beams [Ben-Zvi *et al.* (2004)]), and ultrafast electron microscopy/diffraction (UEM/UED) experiments [Lobastov *et al.* (2005); Sciaini and Miller (2011)].

All alkali-antimonide photocathodes for photon detection and accelerator applications are grown via thermal evaporation of alkali and antimony metals, resulting in either polycrystalline or amorphous thin films [Bates Jr *et al.* (1980)] with disordered surfaces [Musumeci *et al.* (2018)] and in-gap defect states [Spicer (1958)]. Theoretical studies predict that emission of electrons from these defect states and scattering of electrons from disordered surfaces during emission adversely impact the photoemission properties of quantum efficiency and mean transverse energy from these cathodes [Saha *et al.* (2023)]. This limits the efficiency of photon detectors and the maximum possible brightness in accelerator applications. One way to address this issue is to develop techniques to grow single-crystalline, defect-free thin films of these materials with ordered surfaces.

Although single-crystalline epitaxial Cs_3Sb cathodes have been demonstrated by Parzyck *et al.* (2022) recently, the growth process is fairly complex and involves deposition at a low temperature and annealing at a higher temperature in order to facilitate re-crystallization. Moreover, the reproducibility of results via this growth technique is non-trivial, and the defect density in the bulk and the surface roughness achieved from this growth process is also not well understood. This emphasizes the need for a simpler and more reproducible technique for the growth of single-crystalline, epitaxial alkali-antimonide photocathodes.

One significant factor which could potentially hinder an epitaxial growth of alkali-antimonides (for example, Cs_3Sb) performed via thermal evaporation of sources, is a surface mobility mismatch between constituent atomic species. High surface mobility is often achieved by using a high substrate temperature in the several 100°C range for many epitaxially grown films. However, the dissociation temperature of Cs_3Sb films is well below

64

250°C [Ding *et al.* (2017)] and hence, the growth has to be performed at significantly lower substrate temperature in the several 10°C range. These lower temperatures put a severe constraint on the mobility of antimony (Sb) atoms.

An alternate method to improve the surface mobility and reconstruction without raising the substrate temperature is the ion-beam-assisted molecular-beam-epitaxy (IBA-MBE) technique. In this technique, the growing film is irradiated with hyperthermal ions (E > 1 eV) along with low thermal energy atoms (E < 1 eV). This stimulates the growth via ballistic enhancement of mobility [Trushin *et al.* (2008)]. The underlying idea behind this technique is that the hyperthermal ion bombardment imparts enough energy to overcome the surface displacement energy but not the bulk displacement energy, and causes atoms to get detached from the top of growing islands, resulting in a reduction of cluster height and an increase of cluster width. This marks a transition of the growth process from a three-dimensional island mode to a two-dimensional layer-by-layer epitaxial growth mode. The IBA-MBE technique has been demonstrated to successfully yield GaN films of high crystalline quality on multiple substrates like Al_2O_3 [Gerlach *et al.* (2003)], 6H-SiC [Neumann *et al.* (2012)] and γ-LiAlO$_2$ [Gerlach *et al.* (2007)].

In this paper, we demonstrate our efforts to grow Cs_3Sb cathodes with a reasonably good QE via the IBA-MBE technique. Instead of routinely used thermal Cs sources in the form of SAES strips [SAE (2023)], alkali-azides [Cultrera *et al.* (2014)], pure metallic Cs [Cultrera *et al.* (2016)], SAES alkali metal dispenser [Feng *et al.* (2017)] and SAES cesium molybdate pellets [Saha *et al.* (2022)], we have used a hyperthermal Cs^+ ion gun designed and manufactured by Kimball Physics. Bombardment of the growing film with energetic Cs^+ ions provides hyperthermal kinetic energies, which can improve the antimony mobility without the need to raise the substrate temperature. In Section II, we discuss the working principle and different operating parameters used for the Cs^+ ion gun. In Section III, we discuss the deposition technique that we have used to grow Cs_3Sb cathodes using the

65

Cs$^+$ ion gun. This technique differs significantly from the standard sequential deposition technique and is more aligned with a layer-by-layer growth technique. We then present a spectral response data of QE from Cs$_3$Sb cathode grown on a Si substrate. We conclude with a brief summary and future steps in Section IV.

5.3   Experimental Setup

The ultra-high-vacuum (UHV) chamber used for the growth of Cs$_3$Sb cathodes is equipped with a substrate heater, a quartz crystal microbalance (QCM) to measure the atomic fluxes, an effusion cell for pure metallic antimony (99.9999 % pure antimony shot, Alfa Aesar), and an ILG-6 Cs$^+$ ion gun [ion (2023)] designed and manufactured by Kimball Physics. This growth chamber has been used in the past to grow ultra-smooth alkali-antimonide photocathodes using thermal evaporation of sources [Feng *et al.* (2017); Saha *et al.* (2022)]. A base pressure in the low 10^{-10} torr regime is maintained inside the deposition/growth chamber using a 210 l/s turbo pump.

The sample holder is radiatively heated with an electrical heating element, which is placed a few millimeters away from the back of the substrate. Temperature of the substrate is monitored using a Type K thermocouple connected to the manipulator, which has been previously calibrated with a Type K thermocouple connected directly to the sample holder.

The sample holder is also electrically insulated from the walls of the chamber, allowing the substrate to be negatively biased, to allow emission of electrons from the cathode when illuminated with laser light. A continuous wave laser with 532 nm wavelength is incident on the photocathode surface to generate the photoemission current. The current emitted by the photocathode is measured using a picoammeter (Keithley 6517B). The QE deduced from the photocurrent serves as the major feedback for monitoring the growth of Cs$_3$Sb cathodes.

The Cs$^+$ ion gun (ILG-6 IGPS-1016, Kimball Physics) as shown in Fig. 1 is available

66

as a standard gun with a 2¾ CF Flange Multiplexer. It is mounted on our growth chamber such that the end of the ion gun is located at a distance of approximately 10 cm from the sample holder. Alkali metal Cs is produced via a clean solid-solid chemical reaction. This reaction is triggered by heating a cesium-aluminosilicate alloy by passing a source current through a filament embedded in the gun. It is then surface ionized, accelerated, and focused. The ion gun also has a deflector capability, which allows rapid shut off.

The ion gun was baked along with the rest of the growth chamber to achieve a pressure in the low 10^{-10} torr range. After the bake, the ion gun was turned on and outgassed by ramping the source current gradually to the maximum allowed value of 1.65 A. The Residual Gas Analyzer (RGA) (Stanford Research Systems RGA200) spectrum was monitored during the outgassing process to detect unwanted or unusual element peak, if any. The mass spectrum as shown in Fig. 5.1 was mostly hydrogen dominated with water vapor in the mid 10^{-11} torr range. The 133 amu Cs peak could not be detected by the RGA, which could be either due to the Cs^+ ions being out of line of sight of the RGA or due to an extremely low flux rate.

The key performance metrics for an ion gun for IBA-MBE are the ion flux and the resolution/size of the ion beam. The ion current density is primarily controlled by the ion source by tuning the ion source current and beam energy parameters. The size of the beam spot can be controlled by the focusing voltage. A range of operating values for the different above mentioned parameters was provided by Kimball Physics. Table 5.1 lists the values of the ion gun parameters that were used in our setup to maximize the beam current measured at the location of the sample holder, which is at a distance of about 10 cm from the opening of the ion gun. The different parameters have been optimized based on the working distance in our growth chamber and the area of the sample holder, and will most likely vary from one UHV chamber to another.

The size of an ion beam spot can be estimated by sweeping the ion beam across a
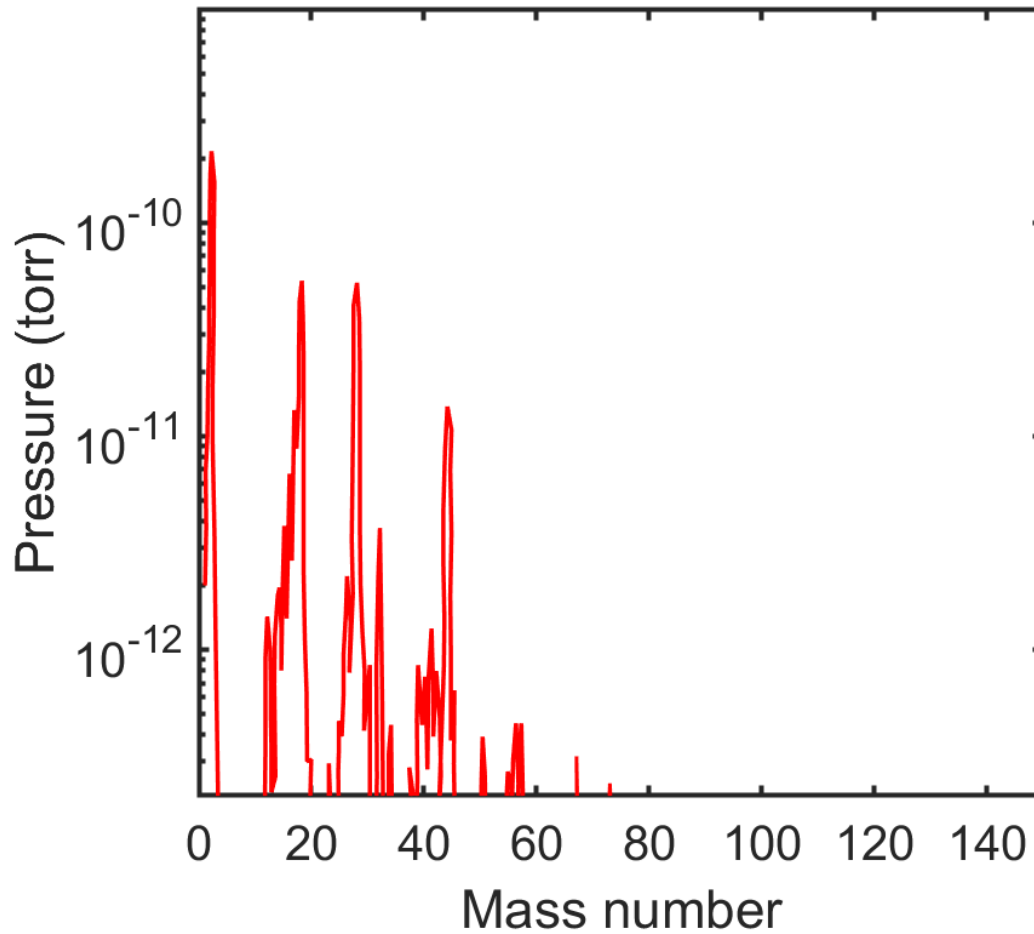
Figure 5.1: RGA Mass Spectrum: Mostly Hydrogen Dominated with Water Vapor in the 10^{-11} Torr Range. No Cs Peak (mass number = 133) was Detected.

Parameter	Typical operating range	Value used
Beam energy(eV)	0-1000	10.0
Source current(A)	1.55-1.65	1.645
Grid(V)	0-1000	0
Extract voltage(V)	0-300	80.0
Focus voltage(V)	0-1000	2.0

Table 5.1: Operating Parameters of the Cs^+ Ion Gun and their Values.

discontinuity such as a knife edge; the change in current on the knife edge is measured as a function of the beam position [Orloff (2010)]. In our experiment, we kept the Cs^+ ion beam stationary while the sample holder assembly was moved upwards/downwards in the vertical z-direction to use the lower edge of the sample holder assembly as the 'knife-edge'. The sample holder assembly is over 4 inches long and the upper edge of the sample holder does not intercept the ion beam. The ion beam current as a function of the z-displacement of the sample holder is shown in Fig. 5.2. The magnitude of the ion current is the least when the ion beam has zero overlap with the sample holder and is maximum when the area of overlap between the ion beam and sample holder is the largest. Based on the z-displacement distance it takes for the intercepted beam to rise to the maximum value, and based on the shape of the sample holder assembly, the beam spot size has been estimated at 2.5 cm in diameter. No bias was applied to the sample holder during the calibration experiment. When a negative bias is applied to the sample holder, we expect the ion beam to deform and the spot size to shrink; however, it is difficult to estimate the reduction in the existing setup.

Using the values of the measured beam current and the estimated beam spot size, the Cs^+ ion flux rate is calculated to be around 6×10^{10} Cs^+ ions/cm^2/sec at the maximum emission current of 50 nA. The lowest Sb atomic flux is that at the QCM detection limit, 0.01Å/s at an Sb source temperature of 400°C, which corresponds to 3×10^{12} Sb atoms/cm^2/sec. Given the working distance in our deposition chamber, the maximum Cs flux rate is, therefore, lower than the Sb flux rate by two orders of magnitude. Thus sequential deposition is required in this geometry with this Cs^+ ion gun, since growing Cs_3Sb cathodes via the co-deposition technique requires Cs flux rates comparable to or higher than the Sb flux rate.

In the next section, we discuss the different approaches which we have performed to grow Cs_3Sb cathodes using the novel Cs source.
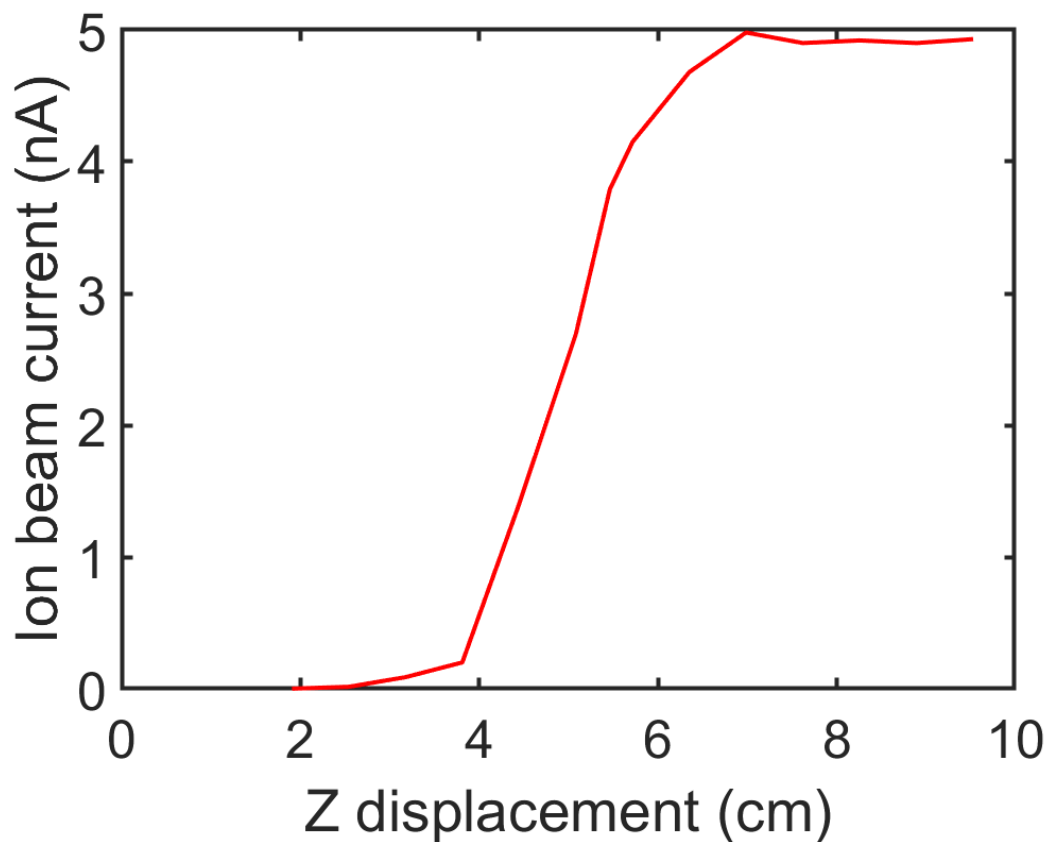
Figure 5.2: Plot of the Ion Beam Current as a Function of the Z-Displacement of the Sample Holder.

5.4 Results and Discussion

Prior to growth, the 10 mm by 10 mm substrates were solvent treated with isopropyl alcohol, followed by annealing at $\sim 450°C$ for 2-3 hours in UHV. The base pressure in the growth chamber was in the range of low 10^{-10} torr. Thereafter, all the growths were performed at room temperature.

The different growth parameters, which were optimized to improve the growth of Cs_3Sb photocathodes, are as follows:

1. thickness of the initial Sb layer,

2. sample-gun potential difference.

A negative potential difference from the Cs gun to the sample provides additional ki-

netic energy to the impinging Cs^+ ions. Too low potential difference will not impart the required kinetic energy to accelerate the incoming Cs^+ ions, whereas a large bias/potential difference may cause the impinging Cs atoms to sputter Sb atoms from the lattice of the growing film. It is therefore crucial to identify the range of potential differences which accelerate Cs^+ ions without sputtering Sb atoms.

5.4.1   Growth 1

Using the Cs^+ ion source, the first Cs_3Sb cathode was grown via the standard sequential technique. The substrate used for this growth was a p-type Si (100) wafer, which was maintained at room temperature to maximize the Cs sticking coefficient. An initial negative bias of 9 V was applied to the back of the sample holder for photocurrent measurements. This is also the sample-gun bias because the gun is at chamber ground.

Sb was deposited on the substrate by heating the pure metallic Sb source for 20 minutes to $400°C$, which corresponds to a thickness of 1.2 nm (or 3.6×10^{15} atoms/cm^2) according to our calibration. After the deposition, the Sb shutter was closed and Sb source heater turned off. The Cs^+ ion gun was turned on and the various parameters on the gun were adjusted to the values specified in the Table 5.1. The ion gun was run continuously at the set parameters for over 72 hours, at which time a photocurrent of the order of 0.1 nA under illumination with a 5 mW green laser was measured. This corresponds to a QE of 5×10^{-6} % in green. Under additional Cs^+ flux, the QE grew to a maximum of 1×10^{-3} % over the span of 24 hours and thereafter, started degrading which is when the growth was terminated by turning the Cs^+ ion gun off.

We expect a total of about 2×10^{16} Cs^+ ions/cm^2 to be incident during this time span of 96 hours (72+24). It is thus greater than 3 times the areal density of Sb, which is more than sufficient for the impinging Cs^+ ions to react with Sb atoms in a 3:1 ratio to form a monolayer of Cs_3Sb. However, the prolonged duration of deposition of Cs^+ ion species

71

(which is necessary owing to the low Cs flux rate) can result in chemical poisoning of the growing cathode film due to the deposition of several monolayers of water and other oxygen-containing species, despite their very low partial pressures in the growth chamber. This could cause an overall slow growth of QE and a lower final QE as compared to that of the Cs_3Sb cathodes grown via thermal deposition of sources. Another reason could be that the ion energy is too high or too low to be compatible with ideal formation of a Cs_3Sb cathode at room temperature. The slow growth does, however, ensure we do not increase the surface temperature more broadly, and thus enables us to decouple the action of the incident ions from any substrate heating effect by the beam.

5.4.2 Growth 2

The rate of growth of QE cannot be improved by increasing the Cs flux rate because it is already at the maximum value that the ion gun can deliver. Instead, we chose to deposit an even thinner layer of Sb in the first place. The Sb layer may act as a reservoir/sponge for alkali metals before they react to form alkali-antimonides [Mamun *et al.* (2015)]. A thinner layer of Sb would require lower amount of alkali metal to form an alkali-antimonide. Thus at very low alkali-metal deposition rates, the alkali-antimonide would form sooner, with a correspondingly lower amount of time for surface contaminants to react and oxidize the alkali metal.

Accordingly, we deposited Sb for 5 minutes, which corresponds to a thickness of 0.3 nm. This thickness is quite low compared to the standard tens of nanometer thick Sb layer usually deposited at the start of sequential deposition of alkali and bi-alkali antimonide photocathodes [Feng *et al.* (2017)]. After the Sb deposition, the Sb shutter was closed and the temperature of the source reduced to room temperature. The Cs^+ ion gun was then turned on and the various operating parameters were set to values specified in Table 5.1.

Fig. 5.3 shows the evolution of QE during the growth of Cs_3Sb cathode on the Si
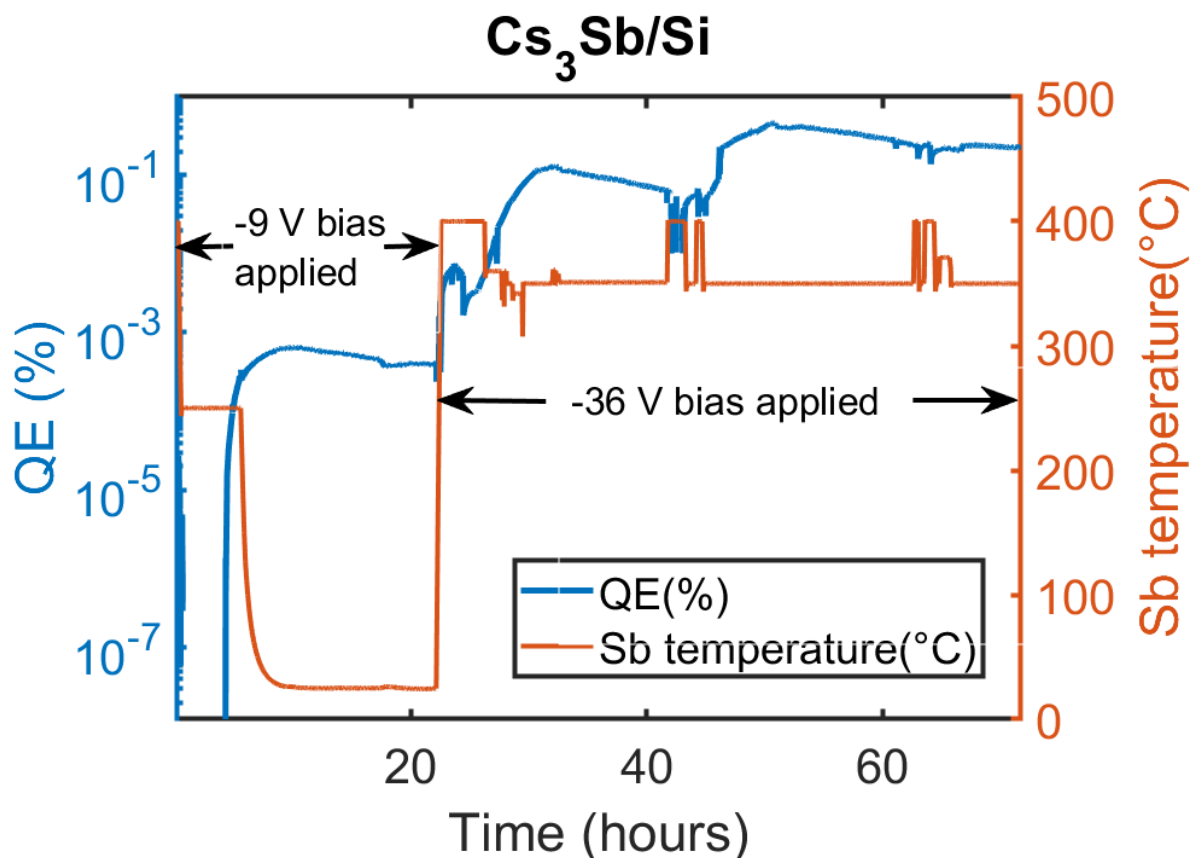
Figure 5.3: Evolution of QE of Cs$_3$Sb Cathode Grown on a Si Substrate at Room Temperature.

substrate. A negative bias of 9 V was initially applied to the back of the sample holder to collect the photocurrent. The QE increased to $2 \times 10^{-3}\%$ in a span of almost a day, contrary to the previous growth in which a lower QE of $1 \times 10^{-3}\%$ was achieved over a duration of 4 days. However, beyond this the QE plateaued.

After this, the bias voltage of the sample was increased from -9 V to -36 V. This imparted the Cs$^+$ ions higher energy as they were striking the surface. Upon increasing the bias voltage, the QE gradually increased to $6 \times 10^{-3}\%$ over the next one hour.

The faster growth of QE observed upon increasing the bias voltage is most likely due to enhancement of mobility of Sb atoms caused by bombardment with more energetic impinging Cs$^+$ ions and can be explained in the following manner. The energy of the Cs$^+$

ions as they exit from the gun is 10 eV, as set by the gun parameter. By application of a negative bias of 36 V, the beam of ions is further accelerated forward towards the sample holder, by a potential difference of 36 V to a total kinetic energy of 46 eV (instead of 19 eV in the case of 9 V battery). The more energetic impinging Cs^+ ions help improve the mobility of Sb atoms by providing the kinetic energy required for the reaction between Sb and Cs atoms to occur, thereby enhancing the kinematics of the chemical reaction of Cs^+ ions with metallic Sb atoms and increasing the evolution rate of QE. The applied voltage was not increased further due to the possibility that the energy of the impinging Cs^+ ions may exceed the bulk displacement energy. In that case, the Sb atoms on the substrate surface would get sputtered away.

After reaching a QE of $6 \times 10^{-3}\%$ in green, the QE began to saturate and eventually drop. This low QE of $6 \times 10^{-3}\%$ could be due to the extremely thin layer of Cs_3Sb cathode grown. The flattening of the growth curve suggests a deficit of Sb atoms in the film to absorb Cs any further, which would be necessary in order to form a thicker layer of Cs_3Sb cathode with higher QE. This entails deposition of a second Sb layer as the next logical step.

Next, we deposited another very thin layer of Sb (thickness being of the order of 0.3 nm) by heating the effusion cell hosting the Sb source to 400°C for 3 minutes. A sharp drop in QE was observed during the Sb deposition as expected, due to the surface condition no longer having low electron affinity. The QE began to recover as soon as the Sb shutter was closed after the completion of the deposition process, presumably due to Cs diffusion or deposition. The Cs^+ ion gun was in the operational mode during the entire course of the deposition process.

The QE increased gradually to a maximum of 0.1% in the span of the next 10 hours, which was followed by a gradual decay. Another round of short Sb deposition was performed when the QE of the Cs_3Sb cathode dropped to half of the maximum value, followed

by Cs^+ ion irradiation for 8 hours . This helped to increase the QE further to 0.45% as can be seen in Fig. 5.3. After reaching a maximum of 0.45%, the QE began to reduce gradually. With further deposition of Sb, we could recover the previous maximum QE of 0.45%; however, the QE could not be maximized any further.
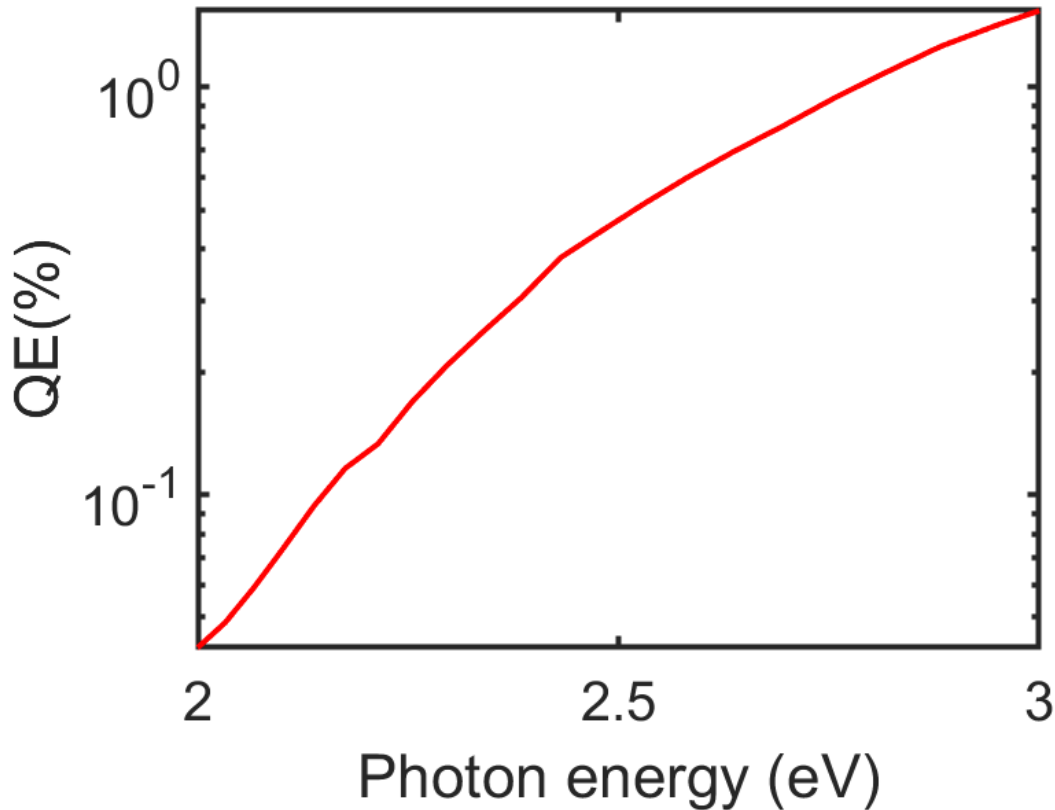
Figure 5.4: Spectral response of QE of the Cs_3Sb Cathode Grown on a Si Substrate Measured During an Intermediate Stage of the Growth, after 48 Hours from the Beginning of the Growth.

The spectral response of QE was measured by shining light from the Optical Parametric Amplifier (OPA), modulated with a mechanical chopper, on the Cs_3Sb cathode, and recording the extracted photocurrent from the cathodes with a lock-in amplifier when a negative bias of 36 V was applied to it. Fig. 5.4 shows the spectral response of QE measured from Cs_3Sb cathode grown on a Si substrate, measured during an intermediate stage of the growth process after 48 hours from the beginning of the growth. The QE was measured to

75

be 0.3% at 532 nm.
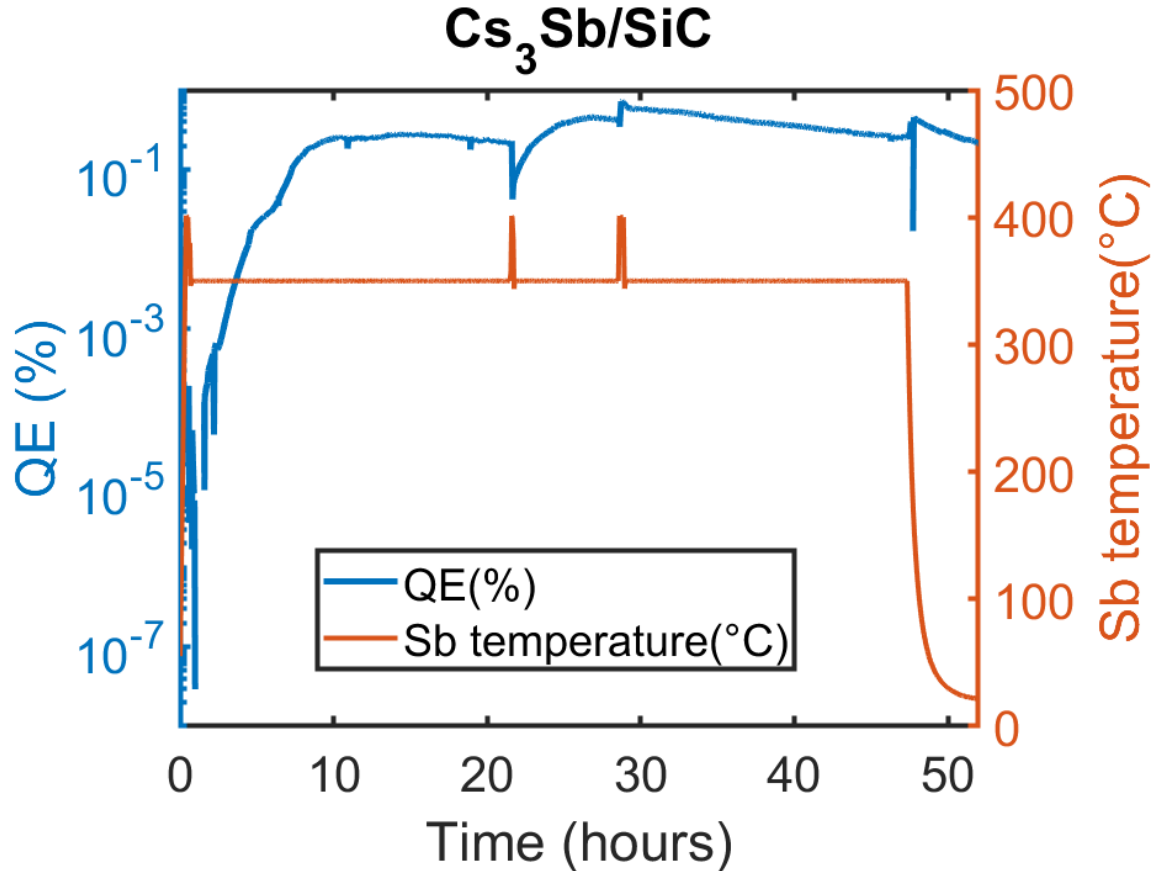
Figure 5.5: Evolution of QE of the Cs_3Sb Cathode Grown on a 3C-SiC Substrate at Room Temperature.

The above recipe, which we have developed to grow Cs_3Sb cathode with Cs^+ ion gun source, was used for growing another Cs_3Sb cathode on a lattice-matched 3C-SiC substrate. The ordered surface of 3C-SiC was prepared by rinsing with isopropyl alcohol followed by annealing the substrate at 450°C in UHV for 3 hours. The growth of QE as a function of time has been reported in Fig. 5.5.

We started with a 0.3 nm thick layer of Sb followed by irradiation with Cs^+ ions till the QE began to saturate at 0.22% in about 20 hours. At that point, the Sb source was heated

76

up to a stable 400°C and the Sb shutter opened for 2 minutes, which allowed the deposition of another very thin layer of Sb. The photocurrent was allowed to rise until the QE began to saturate at a higher value of 0.47%, at which point the Sb shutter was re-opened for 2 minutes and the QE increased to a maximum of 0.72% in green. The Cs^+ ion flux was continuously on throughout this process. All the experimental parameters were kept the same in order to reproduce the growth on a 3C-SiC substrate, with the exception of the bias applied to the sample holder at the beginning of the growth. A negative bias of 36 V was applied to the sample holder throughout the growth on the SiC substrate.

5.5   Conclusion

In this paper, we report on the growth of Cs_3Sb cathodes using a novel Cs^+ ion source. We have demonstrated a different approach from the standard process typically used to grow alkali-antimonide photocathodes. A maximum QE of 0.45% in green was achieved for the cathode grown on a Si substrate. The reproducibility of the growth technique has been demonstrated via the growth of the Cs_3Sb film on a lattice-matched 3C-SiC substrate with a maximum of 0.72%.

The low QE obtained via the growth using Cs^+ ion gun can be attributed to the lower flux of the Cs^+ ion gun compared to thermal evaporation sources, and thus a greater sensitivity to surface contamination over tens of hours of growth. Higher current hyperthermal ion guns with large Cs reservoirs which are capable of providing larger Cs^+ ion fluxes for long periods of time are needed in order to test whether IBA-MBE can grow Cs_3Sb cathodes with a higher QE. Nevertheless, our results show that it is possible to use a novel Cs^+ ion source to enable ion-beam-assisted growth of alkali-antimonides, and this could result in a more repeatable, controllable route to epitaxy. A structural characterization of such cathodes via tools such as RHEED and XRD will be necessary in to investigate the role of the ion-beam-assisted growth technique in facilitating the epitaxial, ordered nature of

77

growth of alkali-antimonide photocathodes on lattice-matched substrates.

5.6   Acknowledgements

Chapter 6

CONCLUSION

Physical and chemical surface non-uniformities on alkali-antimonide cathodes presents
a major hurdle in achieving the highest possible electron beam brightness for several parti-
cle accelerator and electron microscopy applications. The performance of electron-beam-
based, state-of-the-art, ultrafast and ultrasmall tools like X-Ray Free Electron Lasers (XFEL)
and Ultrafast Electron Diffraction (UED) is largely limited by the highest achievable elec-
tron beam brightness. Higher brightness will result in shorter wavelength and more ener-
getic x-ray pulses in the existing XFELs, enabling new experimental capabilities for many
scientific disciplines. An increase in the beam brightness is also crucial for the development
of more accessible, table top, compact XFELs. Increased beam brightness would greatly
help UED applications too, as that would imply an increase in transverse coherence length
of the electrons, which sets an upper limit to the unit cell size of the crystal that can be
imaged greatly increasing the scientific reach of this technique.

In this work, by using lattice-matched Strontium Titanate substrates in conjunction with
co-deposition techniques, we have demonstrated the growth of a high quantum efficiency
Cs_3Sb film. We have measured the topographical and surface potential variations on this
film and shown it to be more than 4 times smoother than the current state-of-the-art. We
show that the surface non-uniformities on such a film are small enough to not have any
conspicuous impact on the brightness of electron beams under any realistic operation con-
dition.

Another reason which could limit the highest possible brightness and lowest possible
MTE was thought to be the defect density of states in the bulk of the alkali-antimonide pho-
tocathodes. Within the framework of Spicer's three-step photoemission theory, we have de-

veloped a new approach to model photoemission from commonly used photocathodes with disordered surfaces, without resorting to any unphysical assumptions. Using this approach, we have explained the near-threshold QE and MTE measurements from alkali-antimonides by the exponentially decaying defect density of states near the valence band maximum. We have shown for the first time that the brightness of electron beams emitted from these cathodes could be limited by the intra-band gap defect density of states.

Despite burgeoning interest in Cs_3Sb cathodes over the years and attempts to characterize their photoemission properties, there has not been a complete, detailed measurement of the kinetic energy distribution, MTE and QE of the Cs_3Sb cathodes in a systematic manner. This is largely due to the complexities of the measurement process coupled with the high susceptibility of the alkali-antimonides to any oxygen-containing species.

We performed the detailed measurements of kinetic energy distribution spectra, MTE and QE of Cs_3Sb cathodes using the photoemission electron microscope (PEEM). The cathodes were transferred via the recently constructed UHV transfer line into the PEEM. Our measurements indicate that the work function of Cs_3Sb cathodes is ~ 1.5 eV, which is much lower than what was deduced from the knee observed in the log plot of the QE spectral response. At the threshold of 1.5 eV, the MTE approaches the thermal limit of 26 meV at room temperature. Our measurements suggest that the higher-than-thermal limit MTE values reported earlier by Cultrera *et al.* (2015) are a consequence of higher excess energy and not due to the surface roughness, the defect density of states as was earlier thought. There is also the signature of scattering losses suffered by the electrons during the transport process to the surface, before emission in the energy distribution spectra as well as the MTE data. However, in addition to low MTE at the threshold, the QE is quite low of the order of 10^{-7} which might limit the operate the near-threshold operation of Cs_3Sb cathodes. Epitaxial, single-crystalline Cs_3Sb cathodes may, however, exhibit different photoemission features when operated at the threshold.

Lastly, although the growth of epitaxial Cs_3Sb cathodes has been demonstrated by Parzyck *et al.* (2022), the growth process is fairly complex and non-trivial to reproduce. The surface mobility mismatch between the constituent atomic species is a significant factor, which could potentially hinder an epitaxial growth of Cs_3Sb cathodes. Often, surface mobility is enhanced by raising the substrate temperature in the several hundreds of Celsius range for many epitaxially grown films, which, however, is not possible in the case of Cs_3Sb cathodes. The growths of these cathodes have to be performed at significantly lower substrate temperatures in the several tens of Celsius range, which puts a severe constraint on the mobility of antimony atoms. We have identified an alternate method to improve surface mobility and reconstruction without raising the substrate temperature, which is the ion-beam-assisted molecular-beam-epitaxy (IBA-MBE) technique. In this work, we have demonstrated the growth of Cs_3Sb cathodes using the ion gun instead of the standard routinely used thermal sources. We have demonstrated a different approach from the standard process typically used to grow alkali-antimonide photocathodes. Cs_3Sb cathodes were grown on 2 different substrates: Si and 3C-SiC. For the cathode grown on Si, a maximum QE of 0.45% was achieved. The reproducibility of the growth technique was demonstrated via the growth of the Cs_3Sb cathode on 3C-SiC substrate with a maximum QE of 0.72%. This low QE obtained via the growth using Cs^+ ion gun can be attributed to the lower flux of the Cs^+ ion gun compared to thermal evaporation sources, and thus a greater sensitivity to surface contamination over tens of hours of growth. Higher current hyperthermal ion guns with large Cs reservoirs which are capable of providing larger Cs^+ ion fluxes for long periods of time are needed in order to test whether IBA-MBE can grow Cs_3Sb cathodes with a higher QE. Nevertheless, our results show that it is possible to use a novel Cs^+ ion source to enable ion-beam-assisted growth of alkali-antimonides, and this could result in a more repeatable, controllable route to epitaxy.

Such different routes to epitaxy must be explored to grow alkali and bi-alkali anti-

monides in a more controlled, reproducible manner. While our measurements indicate that the operation of polycrystalline Cs_3Sb cathodes at the threshold may not be feasible due to an extremely low QE, epitaxial alkali and bi-alkali antimonides might exhibit a higher QE and different photoemission properties at the threshold. It would be worthwhile to pursue research in the direction towards growing other alkali-antimonides and performing systematic photoemission studies of those cathodes, which might produce brighter electron beams for various high brightness applications.

REFERENCES

"Future of electron sources", https://science.energy.gov//media/bes/pdf/reports/2017 (2017).

https://www.saesgetters.com/products-functions/products/getters/non-evaporable-getters/coated-strips (2023).

FOCUS-IS-IEF-PEEM, https://www.focus-gmbh.com (2023).

"Cs-pellets", https://www.saesgetters.com/ (2023).

"Effusion cells", https://www.mbe-komponenten.de/products/mbe-components/effusion-cells.php/ (2023).

"iongun", https://www.kimballphysics.com/product/ilg-6-igps-1016/ (2023).

"Sb pellets", https://www.alfa.com/en/ (2023).

"Sto substrates", https://www.mtixtl.com/ (2023).

Bae, J., I. Bazarov, L. Cultrera, J. Maxson, P. Musumeci, X. Shen, S. Karkare and H. Padmore, "Multi-photon photoemission and ultrafast electron heating in cu photocathodes at threshold", TUPML026 (2018).

Bates Jr, C. W., D. D. Gupta, L. Galan and D. Buchanan, "X-ray photoemission studies of cesium antimonide photoemitters", Thin Solid Films **69**, 2, 175–182 (1980).

Bazarov, I. V., B. M. Dunham, Y. Li, X. Liu, D. G. Ouzounov, C. K. Sinclair, F. Hannon and T. Miyajima, "Thermal emittance and response time measurements of negative electron affinity photocathodes", Journal of Applied Physics **103**, 5, 054901 (2008).

Bazarov, I. V., B. M. Dunham and C. K. Sinclair, "Maximum achievable beam brightness from photoinjectors", Physical review letters **102**, 10, 104801 (2009).

Bell, R., *Negative Electron Affinity Devices*, Monographs in electrical and electronic engineering (Oxford University Press, 1973), URL https://books.google.com/books?id=aEx7wgEACAAJ.

Ben-Zvi, I., J. Brennan, A. Burrill, R. Calaga, X. Chang, G. Citver, H. Hahn, M. Harrison, A. Hershcovitch, A. Jain *et al.*, "R&d towards cooling of the rhic collider", Nuclear Instruments and Methods in Physics Research Section A: Accelerators, Spectrometers, Detectors and Associated Equipment **532**, 1-2, 177–183 (2004).

Bergund, C. N. and W. E. Spicer, "Photoemission studies of copper and silver: Theory", Phys. Rev. **136**, A1030 (1964).

Chubenko, O., S. Karkare, D. A. Dimitrov, J. K. Bae, L. Cultrera, I. Bazarov and A. Afanasev, "Monte carlo modeling of spin-polarized photoemission from p-doped bulk gaas", J. Appl. Phys. **130**, 063101 (2021).

Cultrera, L., I. Bazarov, A. Bartnik, B. Dunham, S. Karkare, R. Merluzzi and M. Nichols, "Thermal emittance and response time of a cesium antimonide photocathode", Applied Physics Letters **99**, 15, 152110 (2011).

REFERENCES

Cultrera, L., M. Brown, S. Karkare, W. Schaff, I. Bazarov and B. Dunham, "Alkali azide based growth of high quantum efficiency photocathodes", Journal of Vacuum Science & Technology B, Nanotechnology and Microelectronics: Materials, Processing, Measurement, and Phenomena **32**, 3, 031211 (2014).

Cultrera, L., C. Gulliford, A. Bartnik, H. Lee, and I. Bazarov, "Ultra low emittance electron beams from multi-alkali antimonide photocathode operated with infrared light", Appl. Phys. Lett. **108**, 134105 (2016a).

Cultrera, L., S. Karkare, H. Lee, X. Liu, I. Bazarov and B. Dunham, "Cold electron beams from cryocooled, alkali antimonide photocathodes", Physical Review Special Topics-Accelerators and Beams **18**, 11, 113401 (2015).

Cultrera, L., H. Lee and I. Bazarov, "Alkali antimonides photocathodes growth using pure metals evaporation from effusion cells", Journal of Vacuum Science & Technology B, Nanotechnology and Microelectronics: Materials, Processing, Measurement, and Phenomena **34**, 1, 011202 (2016b).

Ding, Z., S. Karkare, J. Feng, D. Filippetto, M. Johnson, S. Virostek, F. Sannibale, J. Nasiatka, M. Gaowei, J. Sinsheimer *et al.*, "Temperature-dependent quantum efficiency degradation of k-cs-sb bialkali antimonide photocathodes grown by a triple-element codeposition method", Physical Review Accelerators and Beams **20**, 11, 113401 (2017).

Dowell, D., I. Bazarov, B. Dunham, K. Harkay, C. Hernandez-Garcia, R. Legg, H. Padmore, T. Rao, J. Smedley and W. Wan, "Cathode r&d for future light sources", Nuclear Instruments and Methods in Physics Research Section A: Accelerators, Spectrometers, Detectors and Associated Equipment **622**, 3, 685–697 (2010).

Dowell, D. H., F. K. King, R. E. Kirby, J. F. Schmerge and J. M. Smedley, "In situ cleaning of metal cathodes using a hydrogen ion beam", Physical Review Special Topics-Accelerators and Beams **9**, 6, 063502 (2006).

Dowell, D. H. and J. F. Schmerge, "Quantum efficiency and thermal emittance of metal photocathodes", Phys. Rev. ST Accel. Beams. **12**, 074201 (2009).

Dunham, B., J. Barley, A. Bartnik, I. Bazarov, L. Cultrera, J. Dobbins, G. Hoffstaetter, B. Johnson, R. Kaplan, S. Karkare *et al.*, "Record high-average current from a high-brightness photoinjector", Applied Physics Letters **102**, 3, 034105 (2013).

Emma, P., R. Akre, J. Arthur, R. Bionta, C. Bostedt, J. Bozek, A. Brachmann, P. Bucksbaum, R. Coffee, F.-J. Decker *et al.*, "First lasing and operation of an ångstrom-wavelength free-electron laser", nature photonics **4**, 9, 641–647 (2010).

Feng, J., S. Karkare, J. Nasiatka, S. Schubert, J. Smedley and H. Padmore, "Near atomically smooth alkali antimonide photocathode thin films", Journal of Applied Physics **121**, 4, 044904 (2017).

Feng, J., J. Nasiatka, W. Wan, S. Karkare, J. Smedley and H. A. Padmore, "Thermal limit to the intrinsic emittance from metal photocathodes", Applied Physics Letters **107**, 13, 134101 (2015).

REFERENCES

Ferrario, M., "Overview of fel injectors, 2015", Proc.of EPAC, Edinburgh, Scotland (2015).

Gerlach, J., A. Hofmann, T. Höche and B. Rauschenbach, "Control of the crystalline quality of wurtzitic gan films deposited on γ-lialo2 by ion-beam assisted molecular-beam epitaxy", Nuclear Instruments and Methods in Physics Research Section B: Beam Interactions with Materials and Atoms **257**, 1-2, 315–319 (2007).

Gerlach, J., S. Sienz, W. Attenberger and B. Rauschenbach, "Competition of epitaxy and ion beam irradiation-determined texture during ion beam-assisted deposition of gallium nitride films on r-plane sapphire", physica status solidi (c) , 1, 161–165 (2003).

Gevorkyan, G. S., S. Karkare, S. Emamian, I. V. Bazarov and H. A. Padmore, "Effects of physical and chemical surface roughness on the brightness of electron beams from photocathodes", Phys. Rev. Accel. Beams. **21**, 093401 (2018).

Gordon, M., S. B. van der Geer, J. M. Maxson and Y. K. Kim, "Point-to-point coulomb effects in high brightness photoelectron beam lines for ultrafast electron diffraction", Phys. Rev. Accel. Beams. **24**, 084202 (2021).

Gruner, S. M., D. Bilderback, I. Bazarov, K. Finkelstein, G. Krafft, L. Merminga, H. Padamsee, Q. Shen, C. Sinclair and M. Tigner, "Energy recovery linacs as synchrotron radiation sources", Review of Scientific Instruments **73**, 3, 1402–1406 (2002).

Gupta, P., L. Cultrera and I. Bazarov, "Monte carlo simulations of electron photoemission from cesium antimonide", J. Appl. Phys. **121**, 215702 (2017).

Hagino, M. and T. Takahashi, "Thickness of cs-sb films relative to the original sb films", J. Appl. Phys. **37**, 10 (1966).

Hertz, H., "Ueber einen einfluss des ultravioletten lichtes auf die electrische entladung", Annalen der Physik **267**, 8, 983–1000 (1887).

Hüfner, S., "Photoelectron spectroscopy, principles and applications", URL https://link.springer.com/book/10.1007/978-3-662-09280-4/ (2003).

Jensen, K. L., J. J. Petillo, E. J. Montgomery, Z. Pan, D. W. Feldman, P. G. O'Shea, N. A. Moody, M. Cahay, J. E. Yater and J. L. Shaw, "Application of a general electron emission equation to surface nonuniformity and current density variation", Journal of Vacuum Science & Technology B: Microelectronics and Nanometer Structures Processing, Measurement, and Phenomena **26**, 2, 831–837 (2008).

Kachwala, A., O. Chubenko, D. Kim, E. Simakov and S. Karkare, "Quantum efficiency, photoemission energy spectra, and mean transverse energy of ultrananocrystalline diamond photocathode", Journal of Applied Physics **132**, 22, 224901 (2022).

Karkare, S., G. Adhikari, W. A. Schroeder, J. K. Nangoi, T. Arias, J. Maxson and H. Padmore, "Ultracold electrons via near-threshold photoemission from single-crystal cu (100)", Physical review letters **125**, 5, 054801 (2020).

Karkare, S. and I. Bazarov, "Effects of surface nonuniformities on the mean transverse energy from photocathodes", Physical Review Applied **4**, 2, 024015 (2015).

REFERENCES

Karkare, S., D. Dimitrov, W. Schaff, L. Cultrera, A. Bartnik, X. Liu, E. Sawyer, T. Esposito and I. Bazarov, "Monte carlo charge transport and photoemission from negative electron affinity gaas photocathodes", Journal of Applied Physics **113**, 10, 104904 (2013).

Kiziroglou, M., X. Li, A. Zhukov, P. De Groot and C. De Groot, "Thermionic field emission at electrodeposited ni–si schottky barriers", Solid-State Electronics **52**, 7, 1032–1038 (2008).

Knill, C. J., H. A. Padmore and S. Karkare, "Near-threshold nonlinear photoemission from cu(100)", Proceedings of the 9th International Particle Accelerator Conference, (2021) paper WEPAB099 (2021).

Knill, C. J., H. Yamaguchi, K. Kawahara, G. Wang, E. Batista, P. Yang, H. Ago, N. Moody and S. Karkare, "Near-threshold photoemission from graphene-coated cu (110)", Physical Review Applied **19**, 1, 014015 (2023).

Lobastov, V. A., R. Srinivasan and A. H. Zewail, "Four-dimensional ultrafast electron microscopy", Proceedings of the National Academy of Sciences **102**, 20, 7069–7073 (2005).

Mamun, M., C. Hernandez-Garcia, M. Poelker and A. Elmustafa, "Correlation of csk2sb photocathode lifetime with antimony thickness", APL materials **3**, 6, 066103 (2015).

Mathew, K., A. K. Singh, J. J. Gabriel, K. Choudhary, S. B. Sinnott, A. V. Davydov, F. Tavazza and R. G. Hennig, "Mpinterfaces: A materials project based python tool for high-throughput computational screening of interfacial systems", Comput. Mater. Sci. **122**, 183 (2016).

Maxson, J., P. Musumeci, L. Cultrera, S. Karkare and H. Padmore, "Ultrafast laser pulse heating of metallic photocathodes and its contribution to intrinsic emittance", Nuclear Instruments and Methods in Physics Research Section A: Accelerators, Spectrometers, Detectors and Associated Equipment **865**, 99–104 (2017).

Maxson, J. M., I. V. Bazarov, W. Wan, H. A. Padmore and C. E. Coleman-Smith, "Fundamental photoemission brightness limit from disorder induced heating", Phys. Rev. Accel. Beams. **15**, 103024 (2013).

Melitz, W., J. Shena, A. C. Kummel and S. Lee, "Kelvin probe force microscopy and its application", Surface Science Reports **66** (2011).

Michizono, S., "The international linear collider", Nature Reviews Physics **1**, 4, 244–245 (2019).

Musumeci, P., J. G. Navarro, J. Rosenzweig, L. Cultrera, I. Bazarov, J. Maxson, S. Karkare and H. Padmore, "Advances in bright electron sources", Nuclear Instruments and Methods in Physics Research Section A: Accelerators, Spectrometers, Detectors and Associated Equipment **907**, 209–220 (2018).

REFERENCES

Nangoi, J., M. Gaowei, A. Galdi, J. Maxson, S. Karkare, J. Smedley and T. Arias, "Ab initio study of the crystal and electronic structure of mono-and bi-alkali antimonides: Stability, goldschmidt-like tolerance factors, and optical properties", arXiv preprint arXiv:2205.14322 (2022).

Neumann, L., J. Gerlach and B. Rauschenbach, "Initial stages of the ion-beam assisted epitaxial gan film growth on 6h-sic (0001)", Thin Solid Films **520**, 11, 3936–3945 (2012).

Nguyena, T. H. and S. K. O'Leary, "The dependence of the fermi level on temperature, doping concentration, and disorder in disordered semiconductors", J. Appl. Phys. **88**, 3479 (2000).

Orloff, J., "Measuring the beam size of a focused ion beam (fib) system", in "Scanning Microscopy 2010", vol. 7729, pp. 36–44 (SPIE, 2010).

Oudheusden, T. V., E. F. de Jong, S. B. van der Geer, W. O. 't Root, O. J. Luiten and B. J. Siwick, "Electron source concept for single-shot sub-100 fs electron diffraction in the 100 kev range", J. Appl. Phys. **102**, 093501 (2007).

Parzyck, C., A. Galdi, J. Nangoi, W. DeBenedetti, J. Balajka, B. Faeth, H. Paik, C. Hu, T. Arias, M. Hines *et al.*, "Single-crystal alkali antimonide photocathodes: High efficiency in the ultrathin limit", Physical Review Letters **128**, 11, 114801 (2022).

Paul, J. T., A. Galdi, C. Parzyck, K. M. Shen, J. M. Maxson and R. G. Hennig, "Computational synthesis of substrates by crystal cleavage", NPJ Comput. Mater. **7** (2021).

Pierce, C. M., J. K. Bae, A. Galdi, L. Cultrera, I. Bazarov and J. Maxson, "Beam brightness from cs–te near the photoemission threshold", Appl. Phys. Lett. **118**, 124101 (2021).

Power, J., "Overview of photoinjectors", in "AIP Conference Proceedings", vol. 1299, pp. 20–28 (American Institute of Physics, 2010).

Rao, T. and D. H. Dowell, *An Engineering Guide to Photoinjectors* (Createspace Independent Publishing Platform, 2013), URL https://doi.org/10.48550/arXiv.1403.7539.

Rosenzweig, J., N. Majernik, R. Robles, G. Andonian, O. Camacho, A. Fukasawa, A. Kogar, G. Lawler, J. Miao, P. Musumeci *et al.*, "An ultra-compact x-ray free-electron laser", New Journal of Physics **22**, 9, 093067 (2020).

Russell, S. J., "Overview of high-brightness, high-average-current photoinjectors for fels", in "Free Electron Lasers 2002", pp. 304–309 (Elsevier, 2003).

Sa-yakanit, V. and H. Glyde, "Urbach tails and disorder", Comments Condens. Matter Phys. **1(13)**, 35–48 (1987).

Saha, P., O. Chubenko, G. S. Gevorkyan, A. Kachwala, C. J. Knill, C. Sarabia-Cardenas, E. Montgomery, S. Poddar, J. T. Paul, R. G. Hennig *et al.*, "Physically and chemically smooth cesium-antimonide photocathodes on single crystal strontium titanate substrates", Applied Physics Letters **120**, 19, 194102 (2022).

REFERENCES

Saha, P., O. Chubenko, J. K. Nangoi, T. Arias, E. Montgomery, S. Poddar, H. A. Padmore and S. Karkare, "Theory of photoemission from cathodes with disordered surfaces", Journal of Applied Physics **133**, 6 (2023).

Sakata, T., "Studies on the cs3sb photo-cathode", Journal of the Physical Society of Japan **8**, 6, 723–730 (1953).

Schmeißer, M. A. H., S. Mistry, H. Kirschner, S. Schubert, A. Jankowiak, T.Kamps and J. Kuhn, "Towards the operation of cs-k-sb photocathodes in superconducting rf photoinjectors", Phys. Rev. Accel. Beams. **21**, 113401 (2018).

Schubert, S., M. Ruiz-Oses, I. Ben-Zvi, T. Kamps, X. Liang, E. Muller, K. Mueller, H. A. Padmore, T. Rao, X. Tong, T. Vecchione and J. Smedley, "Bi-alkali antimonide photocathodes for high brightness accelerators", Appl. Materials **1**, 032119 (2013).

Sciaini, G. and R. D. Miller, "Femtosecond electron diffraction: heralding the era of atomically resolved dynamics", Reports on Progress in Physics **74**, 9, 096101 (2011).

Smedley, J., M. Gaowei, J. Sinsheimer, K. Attenkofer, J. Walsh, J. Kuhn, E. Muller, Z. Ding, H. Frisch, H. Bhandari *et al.*, "Sputter growth of alkali antimonide photocathodes: An in operando materials analysis", in "Proceeding of the 2015 International Particle Accelerator Conference", (2015).

Spicer, W. and A. HerreraGómez, "Modern theory and applications of photocathodes", Proc. SPIE 2022, Photodetectors and Power Meters, (1993).

Spicer, W. E., "Photoemissive, photoconductive, and optical absorption studies of alkali-antimony compounds", Physical review **112**, 1, 114 (1958).

Sun, T., F. A. Koeck, C. Zhu and R. J. Nemanich, "Combined visible light photo-emission and low temperature thermionic emission from nitrogen doped diamond films", Applied Physics Letters **99**, 20, 202101 (2011).

Trushin, Y. V., D. Kulikov, K. Safonov, J. Gerlach, T. Höche and B. Rauschenbach, "Atomic assembly during ion-beam assisted growth: Kinetic modeling", Journal of Applied Physics **103**, 11, 114904 (2008).

Vecchione, T., I. Ben-Zvi, D. H. Dowell, J. Feng, T. Rao, J. Smedley, W. Wan and H. A. Padmore, "A low emittance and high efficiency visible light photocathode for high brightness accelerator-based x-ray light sources", Appl. Phys. Lett. **99**, 034103 (2011).

Vecchione, T., D. Dowell, W. Wan, J. Feng and H. Padmore, "Quantum efficiency and transverse momentum from metals", Proceedings of FEL 2013, New York, NY (2013).

APPENDIX A

AUTHOR DECLARATION

Chapter 2 has been published in the journal, Applied Physics Letters in the year 2022.

Chapter 3 has been published in the Journal of Applied Physics in the year 2023.

All the co-authors have granted permission for me to use the 2 published papers as chapters of my PhD thesis.